STRUCTURAL BIOLOGY

Structures of the 26*S* proteasome in complex with the Hsp70 co-chaperone Bag1 reveal a mechanism for direct substrate transfer

Moisés Maestro-López[1]†, Tat Cheung Cheng[2,3]†, Jimena Muntaner[1]†, Margarita Menéndez[4,5], Melissa Alonso[1], Andreas Schweitzer[3,6], Masato Ishizaka[2], Robert J. Tomko Jr.[7], Jorge Cuéllar[1]*, José María Valpuesta[1]*, Eri Sakata[3,6]*

Coupling between the chaperone and degradation systems, particularly under stress, is essential for eliminating unfolded proteins. The co-chaperone Bag1 links Hsp70 to the 26*S* proteasome, recruiting Hsp70-bound clients for proteasomal degradation. Here, we present cryo–electron microscopy structures of the Bag1-bound 26*S* proteasome, revealing unprecedented conformational rearrangements within the 19*S* regulatory particle. Bag1 binding to the Rpn1 induces a marked reconfiguration of AAA$^+$ adenosine triphosphatase (ATPase) ring, disrupting its canonical spiral staircase and remodeling the central channel architecture. This reconfiguration generates a large cavity above the substrate entry gate of the 20*S* core particle. The conserved pore-2 loops of ATPases Rpt2 and Rpt5 play critical roles in opening of the 20*S* gate, enabling substrate entry into proteolytic chamber independently of ubiquitination. These findings suggest a previously unknown mechanism of the proteasomal degradation, by which remodeling the central cavity and 20*S* gate in the presence of Bag1, possibly bypassing the need for ubiquitination.

INTRODUCTION

The coordination between the chaperone network and protein degradation pathways is crucial for maintaining cellular proteostasis (*1*). Chaperones attempt to refold nascent or abnormal proteins and solubilize aggregated proteins, but, when they fail to refold, aberrant proteins are eliminated through regulated degradation (*2*, *3*). In the ubiquitin (Ub)–proteasome system, covalent conjugation of polyubiquitin chains on substrates directs specific protein degradation by the 26*S* proteasome (*3*, *4*). The degradation process starts with the recognition of ubiquitinated substrates by the 19*S* regulatory particle (RP), followed by their unfolding and translocation through a central channel into the proteolytic chamber of the 20*S* core particle (CP) (*4*, *5*). Six AAA$^+$ adenosine triphosphatase (ATPase) subunits, Rpt1-6, unfold substrates by processive threading through the central channel, fueled by sequential adenosine 5′-triphosphate (ATP) hydrolysis (*6*–*8*). Proteasome function is finely tuned by transiently associated cofactors, as represented by Ub-like (UBL)-Ub-associated proteins (Rad23 and Dsk2/Ubqln), which help to recruit polyubiquitinated substrates to the 26*S* proteasome (*9*). The UBL domain can be found in other proteasome cofactors with different functions, including the deubiquitinating enzyme (DUB) Ubp6/Usp14 (*10*) and the Hsp70 co-chaperone Bcl-2–associated anthanogene 1 (Bag1) (*11*).

Besides the degradation of ubiquitinated proteins, the proteasome can also process certain proteins through Ub-independent pathways. For example, unfolded proteins (*12*, *13*), intrinsically disordered proteins (IDPs) (*14*, *15*), and some specific regulatory proteins, which require rapid turnover during signal and stress responses (*16*–*18*), have been reported to be eliminated through Ub-independent mechanisms, sometimes with the assistance of adaptor proteins. However, the precise mechanisms by which the 26*S* proteasome executes Ub-independent degradation remain poorly understood.

Hsp70s are a large family of chaperones that use an ATP-driven conformational cycle to recognize misfolded proteins, promote refolding, and prevent/resolubilize protein aggregation (*1*–*3*). Hsp70s contain two highly conserved domains, the nucleotide-binding domain ($Hsp70_{NBD}$) and the substrate-binding domain ($Hsp70_{SBD}$) (fig. S1A). The Hsp70 ATP/adenosine 5′-diphosphate (ADP) cycle is regulated by two distinct protein families: Hsp40s, which induce ATP hydrolysis, and nucleotide exchange factors (NEFs), which facilitate the ADP/ATP exchange (*2*, *19*, *20*). One of these NEFs is Bag1 and was initially identified as a binding partner of the anti-apoptotic protein Bcl-2 (*21*). Bag1, which has been shown later to interact with Hsp70 (*22*, *23*), is involved in a wide range of cellular pathways, including proteostasis, apoptosis, DNA transcription, proliferation, and neuronal homeostasis (*24*–*27*). Bag1 contains UBL ($Bag1_{UBL}$) and BAG ($Bag1_{BD}$) domains (fig. S1A); it interacts with the 26*S* proteasome through $Bag1_{UBL}$ and with $Hsp70_{NBD}$ through $Bag1_{BD}$ (*11*).

Although the mechanism by which the proteasome degrades ubiquitinated proteins has been structurally elucidated (*6*, *7*), it remains uncertain how the 26*S* proteasome, assisted by Bag1, translocates Hsp70 clients into the CP. Here, we report cryo–electron microscopy (cryo-EM) structures of the Bag1-bound 26*S* proteasome. These structures reveal that Bag1 plays a key role in the structural and functional regulation of the 26*S* proteasome. Our results demonstrate that Bag1 not only physically links Hsp70 to the proteasome through Rpn1, thus facilitating delivery of client proteins to

[1]Centro Nacional de Biotecnología (CNB-CSIC), 28049 Madrid, Spain. [2]Institute for Neuropathology, University Medical Center Göttingen, 37073 Göttingen, Germany. [3]Multiscale Bioimaging: From Molecular Machines to Networks of Excitable Cells (MBExC), University of Göttingen, 37073 Göttingen, Germany. [4]Instituto de Química-Física Blas Cabrera (IQF-CSIC), 28006 Madrid, Spain. [5]CIBER de Enfermedades Respiratorias (CIBERES; ISCIII), 28029 Madrid, Spain. [6]Institute for Auditory Neuroscience, University Medical Center Göttingen, 37073 Göttingen, Germany. [7]Department of Biomedical Sciences, Florida State University College of Medicine, Tallahassee, FL 32306, USA.
*Corresponding author. Email: jcuellar@cnb.csic.es (J.C.); jmv@cnb.csic.es (J.M.V.); eri.sakata@med.uni-goettingen.de (E.S.)
†These authors contributed equally to this work.

the proteasome, but also triggers a series of conformational alternations within the proteasome RP. These reconfigurations suggest that client proteins can be degraded independently of ubiquitination and potentially without ATPase motor activity.

RESULTS

The Hsp70–co-chaperone Bag1 interacts with the proteasome subunit Rpn1

We first used size exclusion chromatography (SEC) to test whether Bag1 directly interacts with any of the Ub receptors of the proteasome (Rpn1, Rpn10, and Rpn13 subunits). Bag1 forms a complex with Rpn1 through the UBL domain (Fig. 1A and fig. S1C), but not with Rpn10 (fig. S1D) or Rpn13 (fig. S1E). Rpn1 is composed of an N-terminal domain ($Rpn1_{NTD}$), a C-terminal domain ($Rpn1_{CTD}$), and a toroidal domain ($Rpn1_{TD}$) with so-called T1 and T2 interfaces which interact with Ub and UBL, respectively (fig. S1, A and B) (*28*). Deletion of the N-terminal Rpn1(1-260) had no impact on Bag1 binding (fig. S1G). Furthermore, formation of a ternary complex consisting of Hsp70, Bag1, and Rpn1 was observed (Fig. 1B), despite of no direct interaction between Hsp70 and Rpn1 (fig. S1F). Isothermal titration calorimetry (ITC) experiments showed that Bag1 had a higher affinity for $Hsp70_{NBD}$ ($K_d \approx 50$ nM) than for Rpn1 [dissociation constant (K_d) ≈ 500 nM] (fig. S2, A to C). Titration of Bag1 with an equimolar mixture of Hsp70 and Rpn1 resulted in the formation of the ternary complex (fig. S2D), confirming that Bag1 is capable of concurrently binding to Hsp70 and Rpn1, as demonstrated by SEC (Fig. 1B and fig. S1H). In the complex with Bag1 and Rpn1, Hsp70 can still recognize unfolded proteins, as indicated by Hsp70 client, reduced and carboxymethylated lactalbumin (RCMLA), being present in SEC analysis (Fig. 1B and fig. S1H) (*29*).

Structural characterization of the $Hsp70_{NBD}$:Bag1:Rpn1 complex

Next, we analyzed by cryo-EM the structure of the ternary complex formed by Hsp70, Bag1, and Rpn1 (Hsp70:Bag1:Rpn1). To reduce the structural heterogeneity of Hsp70 (*30*), we used only $Hsp70_{NBD}$. The complex was further stabilized with the cross-linker bis(sulfosuccinimidyl)suberate (BS3) (fig. S1I). After three-dimensional (3D) classification, we obtained two classes of the $Hsp70_{NBD}$:Bag1:Rpn1 ternary complex with different $Bag1_{UBL}$ orientations (Fig. 1C and figs. S3 and S4A). The interaction between $Hsp70_{NBD}$ and $Bag1_{BD}$ is identical to that observed in the crystal structure of $Hsc70_{NBD}$:$Bag1_{BD}$ (fig. S4B) (*31*). The remaining density, likely corresponding to Rpn1, was too weak to be identified unambiguously due to the structural flexibility (fig. S4C). Cross-linking mass spectrometry (XL-MS) analysis of the full-length Hsp70:Bag1:Rpn1 complex identified multiple inter-protein cross-links among the three components (fig. S4D and table S1). Notably, both $Hsp70_{NBD}$ and $Hsp70_{SBD}$ were predominantly cross-linked to $Rpn1_{TD}$, with fewer interactions with $Rpn1_{NTD}$, leading us to conclude the remaining density in the cryo-EM map corresponds to Rpn1. AlphaFold-Multimer predictions (*32*) of the ternary complex support our structure, showing that Bag1 interacts with $Rpn1_{TD}$ via $Bag1_{UBL}$, mediated by a hydrophobic patch around $Bag1_{UBL}$ Ile76, which is similar to other proteasome binding proteins (figs. S4, E and F, and S10, A and B) (*18*, *28*, *33*, *34*). The structural model of $Hsp70_{NBD}$:Bag1:Rpn1, based on our cryo-EM reconstruction, reveals that $Rpn1_{TD}$ is sandwiched between $Bag1_{BD}$ and $Bag1_{UBL}$ (Fig. 1C and fig. S4).

Cryo-EM structures of the Bag1-bound 26*S* proteasome

Having identified Rpn1 as the Bag1 binder, we next performed cryo-EM analysis of the Bag1-bound 26*S* proteasome stabilized with BS3 (figs. S5 and S6). Unexpectedly, the 26*S*-Bag dataset displayed a more complex conformational landscape compared to the control (26*S*:BS3), as revealed by cryoDRGN analysis (fig. S6, F and G) (*35*). Further 3D classification identified three major conformational states, namely, S_A, S_{BAG1} and S_{BAG2}, while the S_A state predominantly appeared in the control dataset (figs. S5 and S6G). The S_A state (19.3% of cleanup up particles) represents the primary substrate-binding state, which is dominant in the absence of substrates to restrict access to the 20*S* CP (*6*, *7*, *34*). The S_{BAG1} structures (10.6% of cleaned up particles) exhibits substantial ATPase deformation and additional density attached to a relatively stable Rpn1 (Fig. 1D). Further 3D classification of S_{BAG1} particles revealed three subclasses representing different extent of ATPase deformation ($S_{BAG1.1}$, $S_{BAG1.2}$, and $S_{BAG1.3}$) (figs. S5 and S7A). The S_{BAG2} class, which account for nearly half of the total particles in the 26*S*:Bag1 dataset (46.8% of clean up particles), was highly heterogeneous (figs. S5 and S6H), and all subclasses showed ATPase deformation, albeit to a lesser extent than S_{BAG1} (Fig. 2F), accompanied by extensive Rpn1 dynamics (figs. S7, B and C, and S8A). A subclass with better-resolved Rpn1 was refined as the representative of the S_{BAG2} structure. After refinement, we obtained four reconstructions of $S_{BAG1.1}$, $S_{BAG1.2}$, $S_{BAG1.3}$, and S_{BAG2} with overall resolutions of 3.5 to 3.7 Å (figs. S5 to S7).

The observed extra mass in the $S_{BAG1.1\text{-}1.3}$ structures is associated with the T2 site (*28*, *34*) of Rpn1 and was attributed to $Bag1_{UBL}$, which aligned with previous studies (*18*, *34*) (Fig. 1, D and E; and fig. S10, A to C). Due to the extensive flexibility of Rpn1 (fig. S8A), Bag1 density was not observed in S_{BAG2} reconstruction (fig. S7, B and C). However, refinement of one subclass that contains better-resolved Rpn1 allowed us to visualize the $Bag1_{UBL}$ in S_{BAG2} (fig. S8B), suggesting that the apparent absence of Bag1 in S_{BAG2} results from the extensive flexibility of Rpn1. In contrast, the $Bag1_{BD}$ density was not clearly observed in any of four reconstructions. To address this, we performed XL-MS analysis of the reconstituted Hsp70:Bag1:Rpn1:ATPase complex using isolated ATPase ring from yeast. Within this heterobase complex, we identified various cross-links, including Rpn1-Bag1, Bag1-Hsp70, Rpn1-Hsp70, Rpn1-Rpt2, Hsp70-Rpn2, and Hsp70-Rpt2 (table S2), indicating the spatial proximity between $Bag1_{BD}$ and Rpn1, as well as Hsp70 and Rpn1. Subsequently, atomic models of the 26*S*:$Bag1_{UBL}$ complex in the $S_{BAG1.1}$ state were generated.

Dynamic conformational alternation of the AAA^+ ATPases induced by Bag1-binding

S_{BAG} structures showed substantial dissimilarities from previously reported EM maps (Figs. 2 to 4 and figs. S9 and 10) (*28*, *34*). Among previously reported structures, the S_{D4} state represents one of the clearest examples of a gate-opening conformation (*34*), which will be discussed below. Besides, in both the S_{BAG} and S_{D4} states, the pore-2 loop of Rpt2, which is a key element in gate opening, is positioned near the CP, leading us to use the S_{D4} as a reference for the following structural comparison. In the $S_{BAG1.1}$ state, the lid complex tilts ~17.7° anticlockwise and shifts by ~19.8 Å toward the Rpn1 N terminus compared to that in the S_{D4} state (fig. S10D). Rpn1 changes its position, shifting ~15.0 Å and rotating ~14.7° toward the interface connecting the ATPase and origosaccharide-binding (OB) domains of both Rpt1 and Rpt2 (Fig. 2, A and C). The $Rpn1_{TD}$ lies in close proximity to the Rpt1 OB domain, and the $Rpn1_{CTD}$ makes contact with the Rpt2 ATPase domain (Fig. 2C). In canonical proteasomes,

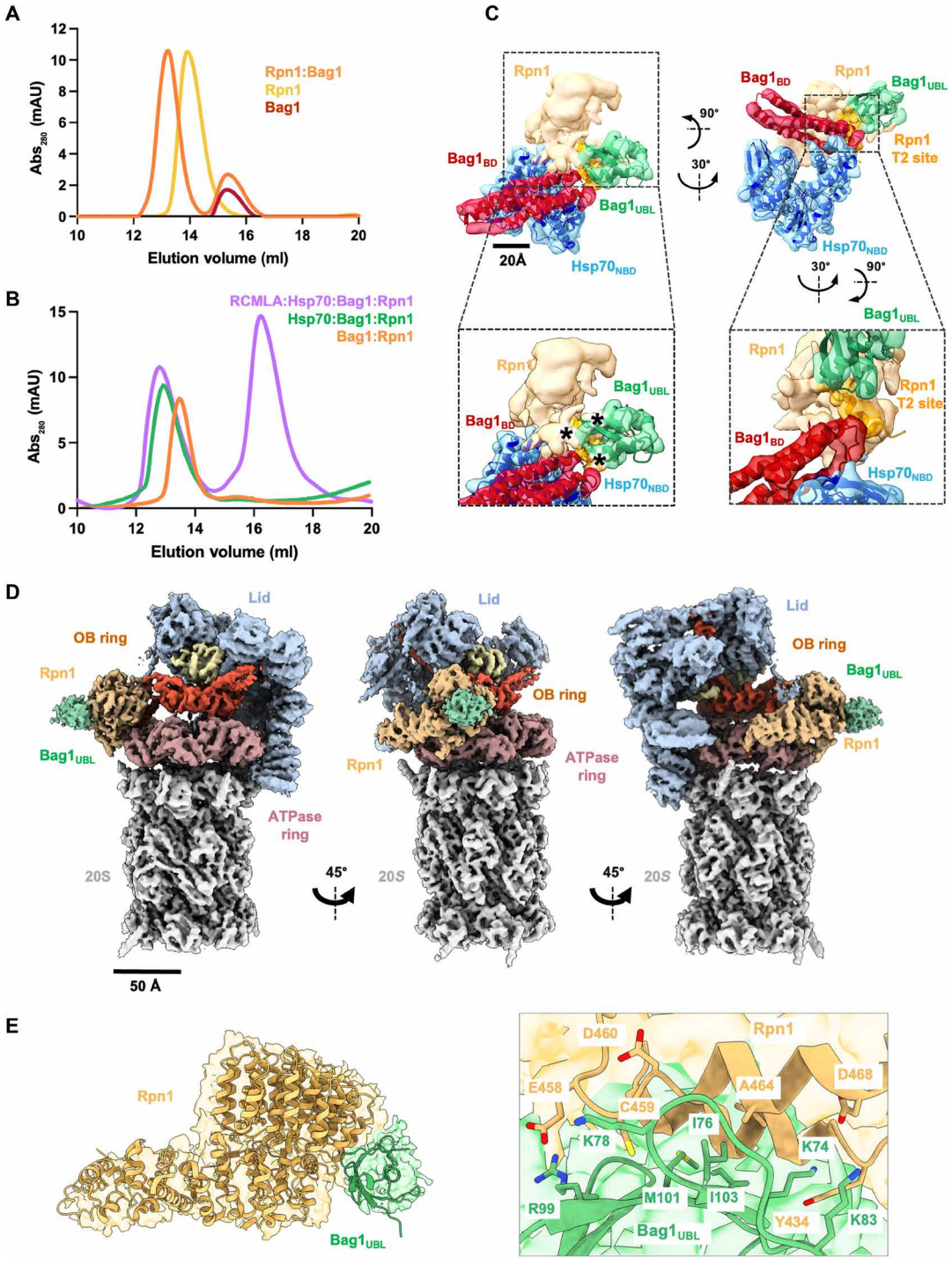

Fig. 1. Bag1 interacts with Rpn1 and Hsp70. (**A**) SEC analysis of the interaction between Bag1 and the proteasome subunit Rpn1. The shift in the elution profile of the sample containing Bag1 and Rpn1 (orange) indicates the formation of a complex compared with Bag1 (red) and Rpn1 (goldenrod) alone. SDS–polyacrylamide gel electrophoresis (PAGE) of the corresponding elution fractions is shown in fig. S1C. (**B**) SEC analysis of the Hsp70-Bag1-Rpn1 complex with a model substrate reduced and carboxymethylated lactalbumin (RCMLA). The sample containing Hsp70, Rpn1, and Bag1 (green) elutes earlier than the Bag1:Rpn1 complex (orange), showing a formation of a ternary complex. Upon addition of RCMLA to the ternary complex (purple), a shift in the elution peak was observed, demonstrating that the model substrate interacts with the ternary complex. SDS-PAGE of the corresponding elution fractions is shown in fig. S1H. (**C**) Different views of the cryo-EM map (4.8-Å resolution) of the $Hsp70_{NBD}$:Bag1:Rpn1 ternary complex. AlphaFold prediction (*32*) of $Hsp70_{NBD}$ (blue) and Bag1 ($Bag1_{BD}$ in red and $Bag1_{UBL}$ in green) was docked into the final map. The remaining density, which is presumably attributed to part of Rpn1, is colored in beige, with the T2 site in goldenrod. Bag1 interfaces to the putative Rpn1 density are indicated with black asterisks. (**D**) Cryo-EM reconstruction of the Bag1-bound 26*S* proteasome in $S_{BAG1.1}$ at 3.6-Å resolution. The $Bag1_{UBL}$ is observed, while the $Bag1_{BD}$ missing in the map due to the structural dynamics of Rpn1 and Bag1. Color codes are as follows: CP (white), ATPase domain (rosy brown), OB domain and coiled-coil (orange), Rpn1 (beige), $Bag1_{UBL}$ (light green), Rpn11 (light yellow), and Lid (light blue). (**E**) Binding of $Bag1_{UBL}$ to the T2 site of Rpn1 in the proteasome. The inset shows contacts between Rpn1 and $Bag1_{UBL}$. All structural figures were created using ChimeraX (*66*).

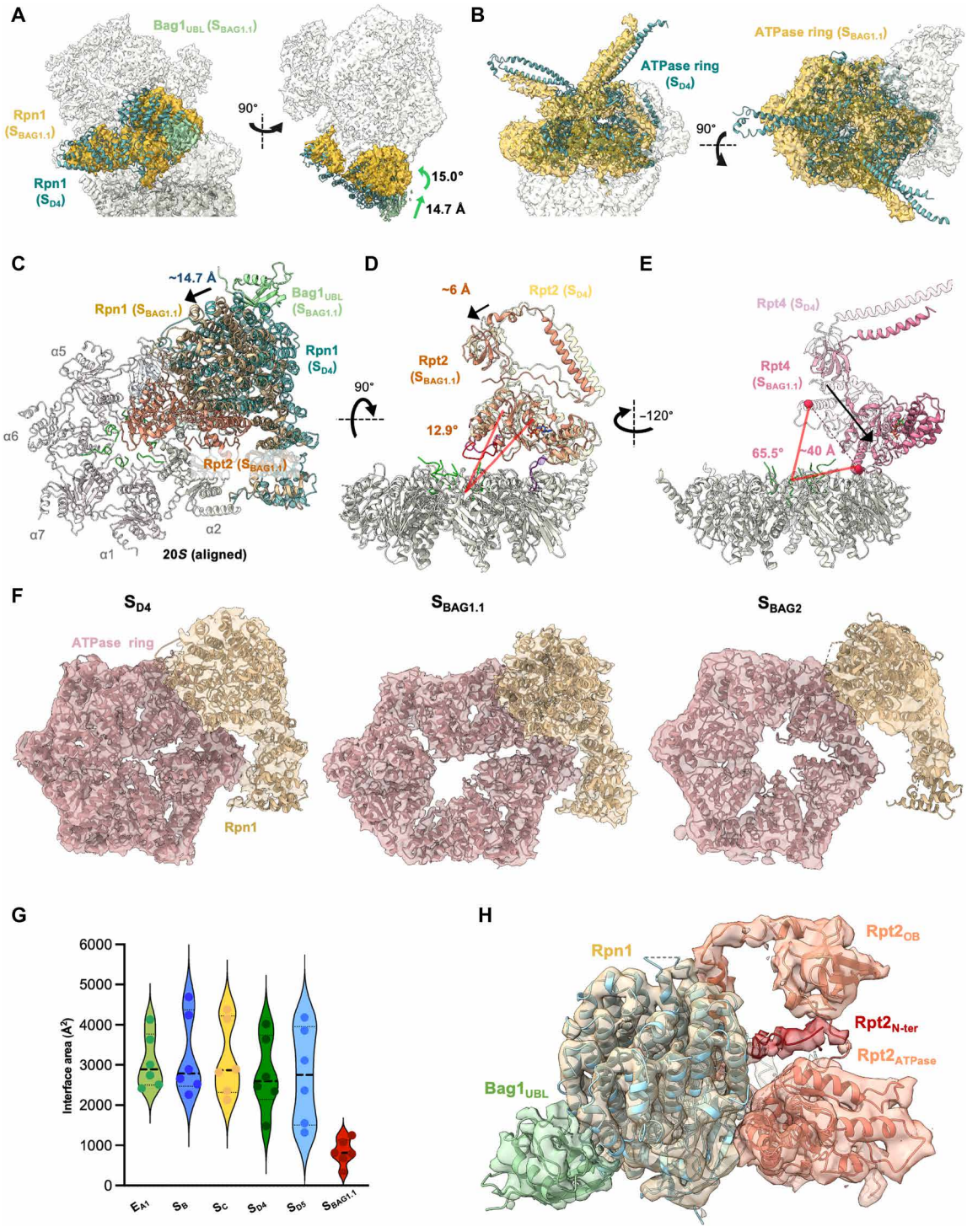

Fig. 2. Dynamic conformational changes of the 26*S* proteasome induced by Bag1. (**A** and **B**) Structural comparison of the cryo-EM reconstruction of the 26*S* proteasome in $S_{BAG1.1}$ with the S_{D4} state [Protein Data Bank (PDB): 7W3K in teal] (*34*), focusing on Rpn1 (A) and the ATPase ring (B). The EM densities of the highlighted subunits in $S_{BAG1.1}$ are shown in gold, and the S_{D4} model is displayed as a ribbon representation. $Bag1_{UBL}$ is shown in light green and the rest of densities are shown in light gray. The changes in shift (angstrom) and angle (degrees) are indicated. (**C** to **E**) Comparison of individual subunits in $S_{BAG1.1}$ and S_{D4} (PDB: 7W3K) states. Structural differences in Rpn1 (C), Rpt2 (D), and Rpt4 (E) are highlighted. Two structures are aligned to the CP α ring. The atomic model of the 20*S* CP is shown in white. Rpn1 is shown in beige for $S_{BAG1.1}$ and in teal for S_{D4} (C). Rpt2 and Rpt4 in $S_{BAG1.1}$ are depicted in salmon and pink, respectively, while the structures in the S_{D4} are shown in transparent [(D) and (E)]. (**F**) Structural comparison of the ATPase ring (rosy brown) and Rpn1 (beige) in the S_{D4} (EMDB: 32282; and PDB: 7W3K), $S_{BAG1.1}$, and S_{BAG2} reveals that the ATPase rings in S_{BAG} are deformed and creates a large cavity at the center. (**G**) Averages of the contact area between the ATPase domains of two adjacent Rpt subunits in different conformational states, calculated by ChimeraX (*66*). Individual values for each structure are shown in dots and the median with a black dashed line. The $S_{BAG1.1}$ has overall contact surfaces 3.5-fold smaller than the other conformational states. (**H**) The Rpt2 N $terminus_{36-41}$ (highlighted in red) shifts from at the interface with Rpn1 toroid domain to the interface between its own OB and ATPase domains, resulting in an enlarged interdomain interface.

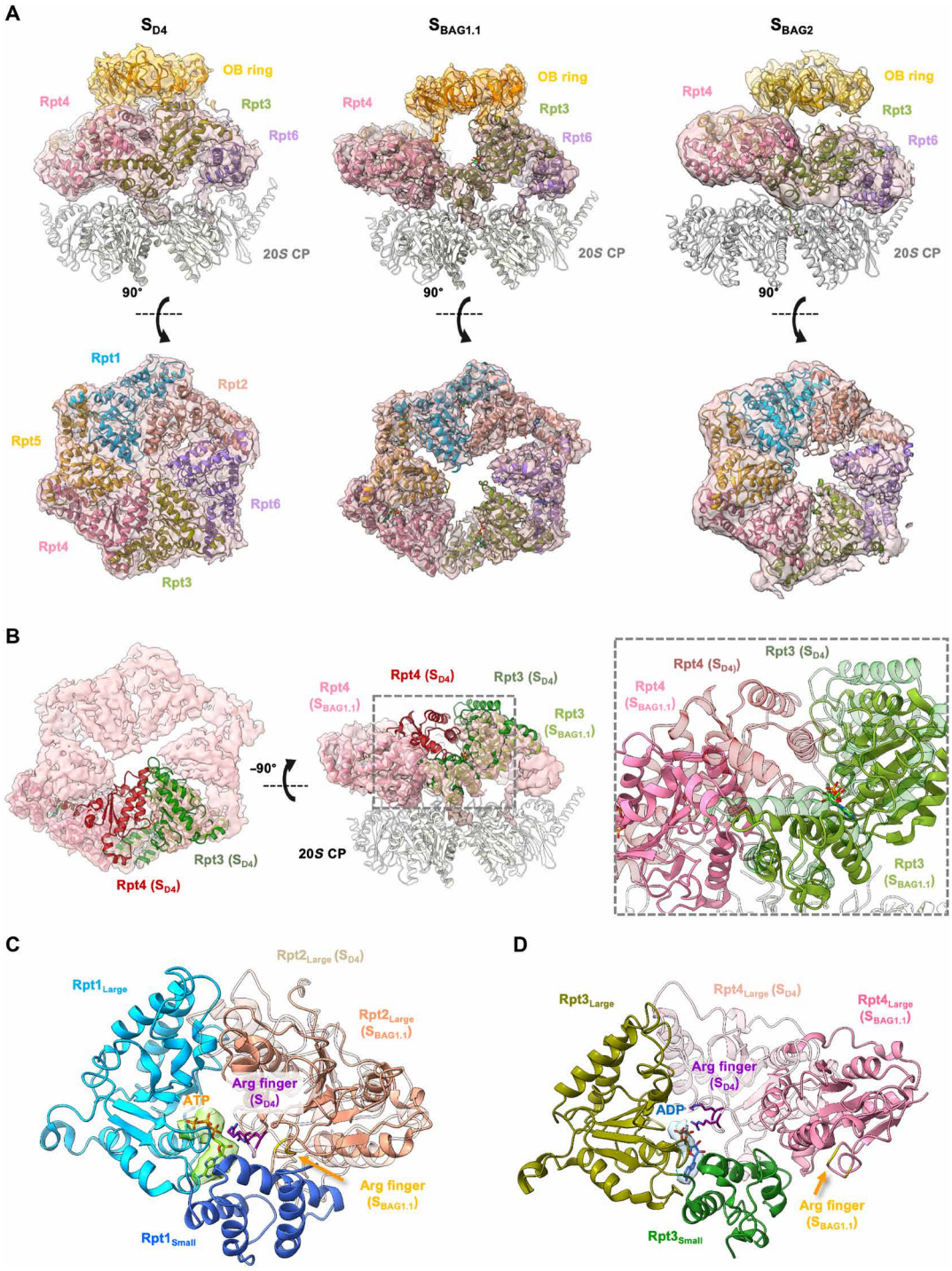

Fig. 3. Deformation of the ATPase ring in S_{BAG}. (**A**) Cross sections of cryo-EM maps in S_{D4} (EMDB: 32282; and PDB: 7W3K) (*34*) and the Bag1-bound conformations, $S_{BAG1.1}$ and S_{BAG2}, focusing on the interface between the OB and ATPase rings (top). Conformational rearrangements within the ATPase ring produce a substantial opening at the OB-ATPase interface. Cryo-EM densities are shown in transparent. Corresponding segmentations of the ATPase rings (bottom) reveal a large central cavity in the Bag1-bound conformations, whereas the ATPase ring is tightly packed in S_{D4}. Atomic models of the subcomplexes and individual Rpt subunits are colored as follows: OB ring (light orange), 20*S* CP (white), Rpt1 (light blue), Rpt2 (salmon), Rpt6 (purple), Rpt3 (green), Rpt4 (hot pink), and Rpt5 (yellow). Structural model of the S_{BAG2} ATPases was created by rigid-body fitting of individual domains. (**B**) Structural comparison between $S_{BAG1.1}$ and S_{D4}, focusing on Rpt3 (olive) and Rpt4 (hot pink) with the S_{D4} structure displayed in transparent. (**C**) Structural comparison of the Rpt2 large domains between $S_{BAG1.1}$ and S_{D4} at the Rpt1 interface. Both structures are superimposed using the Rpt1 large domain (light blue). Only Rpt1 subunit in $S_{BAG1.1}$ is shown (small domains in blue). Rpt2 large domains in $S_{BAG1.1}$ (salmon) and S_{D4} (transparent) reveal a positional shift, with the loop containing the Rpt2 Arg-finger (yellow) located far from the nucleotide in the Rpt1 pocket. Rpt2 Arg-finger in S_{D4} is highlighted. (**D**) Structural comparison of the Rpt4 large domain between $S_{BAG1.1}$ and S_{D4} at the Rpt3 interface. Superposition using the Rpt3 large domain (olive) shows that the Rpt4 large domain in S_{BAG1} shifts by ~40 Å and rotates 65.5° in comparison to S_{D4} (Fig. 2E). Rpt4 Arg-finger in S_{D4} is highlighted. The loop containing Arg-finger (yellow) is positioned far from the nucleotide in the Rpt3 pocket.

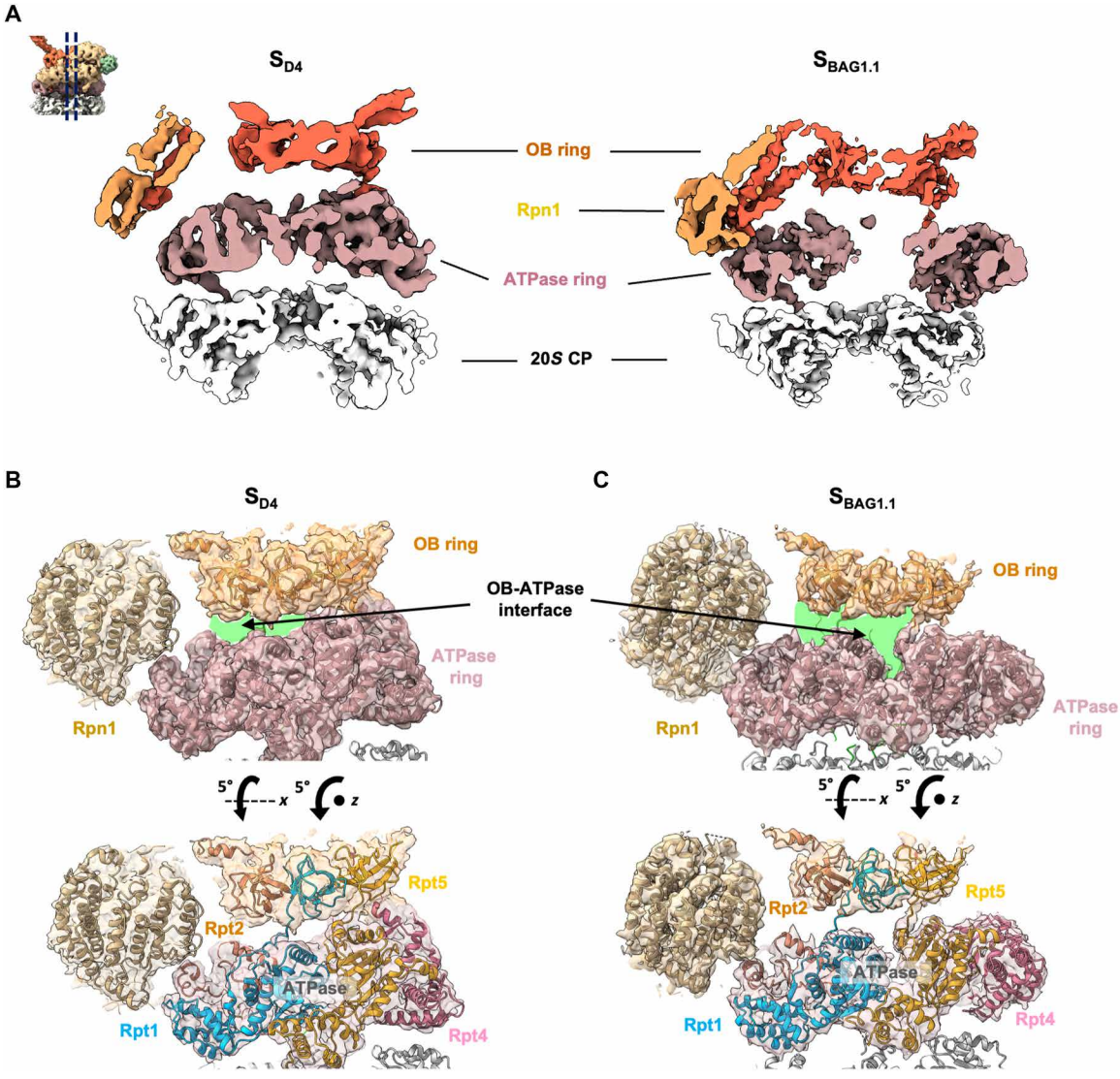

Fig. 4. ATPase subunits are loosely packed in S_{BAG} states. (**A**) Cross section of cryo-EM map of the proteasome in S_{D4} (EMDB: 32282) (*34*) and $S_{BAG1.1}$. Rpn1 (tan), OB ring (orange), ATPase ring (rosy brown), and CP (white) are colored separately. The central channel is open and aligned in the S_{BAG} structures, whereas the interior of the ATPase ring is packed in S_{D4}. The individual EM maps were low-pass filtered to 4 Å of resolution. (**B** and **C**) Cryo-EM maps of the proteasome in S_{D4} (B) and $S_{BAG1.1}$ (C) focusing on the interface between the ATPase and CP rings. In $S_{BAG1.1}$, the atypical positioning of the ATPase subunits creates a large cleft (highlighted in light green) between the OB and ATPase rings. The atomic models of Rpt1, Rpt4, and Rpt5 are colored in light blue, pink, and yellow, respectively.

the Rpt2 N terminus (residues 36 to 41) interacts with the $Rpn1_{TD}$ to regulate its orientation relative to the ATPase ring (fig. S11A). In $S_{BAG1.1}$, the Rpt2 N $terminus_{36\text{-}41}$ is embedded at the OB-ATPase interface (Fig. 2H and fig. S11), which triggers to enlarge its OB-ATPase interface and to drive Rpn1 inward, inducing further conformational changes that deform the ATPase ring (fig. S11). Despite subtle conformational changes in Rpn1 itself (fig. S10E), more marked structural rearrangement is observed in the AAA^+ ATPases in all four S_{BAG} states (Fig. 2, B and D to F, and fig. S9). The ATPase ring no longer retains its spiral staircase conformation but adopts an asymmetric hexameric shape with a an extensive distortion (Figs. 2F and 3A; fig. S9, C and D; and movie S1). This deformation is caused by conformational alternation of all six Rpt subunits, most pointedly with Rpt4 shifting off-center (Fig. 3, B to D, and fig. S12C). The fine architecture of the central channel, where the substrate-binding pore loops are arranged in a staircase, becomes disrupted and deformed, resulting in the formation of a substantial internal cavity at the center of the ring (Figs. 2F, 3, and 4A; fig. S12; and movie S2). In the $S_{BAG1.1}$ structure, the Rpt subunits are positioned at random heights rather than the ordered spiral arrangement seen in the canonical 26*S* structures (fig. S12). Similar distortions including a large cavity were observed in the other three conformations ($S_{BAG1.2}$, $S_{BAG1.3}$, and S_{BAG2}) (Figs. 2F and 3, and figs. S9 and S13), although the shift of the individual Rpt subunits is different among these states. Together, the S_{BAG} structures represent previously unidentified conformations, substantially departing from all proteasome states known to date.

Next, to test whether $Bag1_{UBL}$ alone can induce the observed conformational changes, we analyzed 3D structures of the 26*S* in the presence of the isolated $Bag1_{UBL}$ or $Bag1_{BD}$ domains. However, these

structures remained in S_A (fig. S14), indicating that, in addition to $Bag1_{UBL}$ anchoring Rpn1, $Bag1_{BD}$ is needed to induce the proteasome conformational changes.

The highly conserved packed interfaces between adjacent ATPase subunits, which are regarded as "rigid bodies" in the AAA^+ ATPases (e.g., $S_{A\text{-}D}$, S_{D4}, and $E_{A\text{-}D}$) (*7*, *34*), are widely opened up in $S_{BAG1.1}$, with contact surface areas of ~1000 $Å^2$, markedly smaller than those observed in any of the canonical interfaces with average contact area of 2996 $Å^2$ (Fig. 2G and fig. S12E). In particular, Rpt4, rotated by ~65.5° and shifted by ~40 Å, interacts neither with the Rpt3 large domain nor with its nucleotide-binding site, and maintains only limited contact with the Rpt3 small domain, which covers 331.5 $Å^2$ (Figs. 2E and 3, C and D). The $S_{BAG1.1}$ map shows nucleotide density in all six nucleotide-binding pockets (fig. S12F). However, across all interfaces, the Arg finger motifs, crucial for the interaction with the ATP γ-phosphate of the adjacent subunit, are located far away from the nucleotides in S_{BAG} structures (Fig. 3, C and D, and fig. S12D). We demonstrated that ATPase activity decreased upon full-length Bag1 titration (Fig. 5A). The modest inhibition of the ATPase activity by Bag1 likely results from its transient binding on the 26*S* proteasome. Although a previous study showed that UBL binding does not stimulate the ATPase activity (*36*), $Bag1_{UBL}$ also modestly reduced ATPase activity, while $Bag1_{BD}$ had no effect. Given that $Bag1_{UBL}$ does not induce the ATPase deformation, the unique N-terminal segment of Bag1, which is rich in charged residues, likely contributes to the modulation of ATPase activity. Thus, Bag1 binding deforms the interfaces of the Rpt subunits and blocks the ATPase activity of the 26*S* proteasome.

Mechanism of gate opening by Bag1

Unexpectedly, three $S_{BAG1.1\text{-}1.3}$ structures show open gate conformations with apertures of varying diameter, similar to previous observations in the substrate-bound 26*S* structures (*6*, *7*) (Fig. 5B and fig. S13G). In $S_{BAG1.1}$ and $S_{BAG1.3}$, the N-terminal tails of all α subunits, which form the 20*S* CP gate, adopt an open conformation except for the α3 N terminus (Fig. 5, C and D, and fig. S13G), which shows two conformations: perpendicular (up) or parallel (down) to the CP plane (Fig. 5, C and D), whereas the gate in $S_{BAG1.2}$ is completely open (fig. S13G). The coordinated insertion of the five Rpt C termini (Rpt2, Rpt3, Rpt5, Rpt1, and Rpt6) into the α pockets are critical for gate opening, as observed in S_{D4} (fig. S13G) (*6*, *37*, *38*). In the three $S_{BAG1.1\text{-}1.3}$ structures, only densities of the C termini of three subunits (Rpt2, Rpt3, and Rpt6) are detected in the α pockets, placing the N termini of α1, α2, and α3 in the open-gate conformation (Fig. 5B, fig. S13G, and movie S3). In contrast, the Rpt1 and Rpt5 C termini, which regulate the α4 and α5 N termini, are not observed. Instead, the N termini of the α4 and α5 subunits are held up by their interaction with the Rpt2 pore-2 loop (Fig. 5, E and F, and movie S4). Additionally, the pore-2 loop of Rpt5 supports the α7 N terminus, which further interacts with the α6 N terminus (Fig. 5, G and H, and movie S4). The conserved pore-2 loops in the previous substrate-bound proteasome structure form a spiral staircase below the pore-1 loops, with both loops intercalating into the processing polypeptide within the central channel (*6*, *7*, *34*). The pore-2 loops in the Bag1-bound 26*S* structures, especially Rpt2, Rpt4, and Rpt5, position much closer to the CP compared to those in the canonical structures (Fig. 5, E to H; fig. S12B; and movie S4). Although the Rpt4 pore-2 loop also lowers its position, its density disappears above the α pocket between α7 and α1, thus not allowing us to decipher its role (fig. S12B). In contrast, coupled with its structural heterogeneity of the ATPase ring, the gate-opening states in S_{BAG2} subclasses vary (fig. S8C), although the refined S_{BAG2} reconstruction represents a closed state (fig. S13G).

Last, the shift of the Rpt2 pore-2 loop toward the CP gate is coupled with a global structural change of the Rpt2 subunit, which is induced by a conformational alternation of Bag1-bound Rpn1. Deformation of the ATPase ring impairs the pore loop function for substrate translocation but instead provides a previously unrecognized function, enabling substrate entry into the CP by gate opening (Fig. 5, E to H, and movie S4).

Mechanism of Bag1-induced proteasomal degradation

Bag1-induced deformation of the ATPase ring lowers the individual ATPase subunits, placing them closer to the CP ring. Besides, the respective position of the OB ring and DUB Rpn11 exhibits a slight change (fig. S15, A and B). These conformational changes create a gap of ~20 Å between the OB ring and the ATPase ring (Figs. 3A and 4, A and B; fig. S15, C to H; and movie S4). All OB-ATPase interfaces are loosened compared to those of the canonical proteasome structures, particularly for Rpt4 and Rpt5, which are off-centered and largely protrude from the CP cylinder (fig. S15, C to H). Notably, the wide OB-ATPase opening is interconnected to the prominent cavity at the center of the ATPase rings, reaching the CP gate (Fig. 4). The architecture of this cavity suggests a role as a substrate chute for direct protein degradation.

To understand the biological role of Hsp70:Bag1 binding to the 26*S* proteasome, we fitted the structural model of the $Hsp70_{NBD}$:Bag1:Rpn1 complex (Fig. 1C) into the 26*S*:Bag1 complex. Positioning of $Hsp70_{SBD}$ with respect to $Hsp70_{NBD}$ varies, depending on nucleotide-binding status, cofactor binding, and substrate engagement (*2*). Two Hsp70 structures, an x-ray structure of *Escherichia coli* Hsp70 [Protein Data Bank (PDB): 2KHO] as well as an AlphaFold prediction of ADP-bound Hsp70 are fitted into the complex without clashing with the ATPase ring. The Hsp70 hydrophobic patch that mediates substrate binding can be in close proximity of the OB-ATPase gap created by Rpt4 and Rpt5 (Fig. 6A). Further, our XL-MS analysis of the yeast ATPase ring with Hsp70, Bag1, and Rpn1 identified cross-linkers among these components (table S2), supporting that Bag1 and Hsp70 can be positioned near Rpn1 and Rpt subunits. This structural model suggests an optimal transfer of the unfolded protein directly from Hsp70 to the 20*S* CP chamber for degradation.

The disrupted interface of the nucleotide-binding pockets accounts for the reduced ATPase activity of the proteasome upon Bag1 binding (Fig. 5A), while its peptidase activity was increased by Bag1 binding (fig. S16H). To address whether Bag1 influences the degradation of unstructured proteins, we used α-synuclein (α-syn) as a model substrate, which is a highly expressed IDP in neurons (*39*). Although the observed degradation was relatively slow, probably due to the aggregation-prone nature of α-syn (*40*), the presence of Bag1 enhanced α-syn degradation (Fig. 6B and fig. S16). When combined with Hsp70, Bag1 moderated the degradation rate of α-syn (Fig. 6B and fig. S16). Besides preventing aggregation (*41*), we propose that Hsp70, together with Bag1, selectively guides unstructured substrates to the proteasome by positioning them near the opening between OB and ATPase rings. In contrast, the 20*S* CP alone in the presence of Hsp70 and Bag1 did not show α-syn degradation. Thus, Bag1 can enhance degradation of unstructured proteins by previously unrecognized mechanisms by promoting conformational change within the proteasome in a Ub-independent manner.

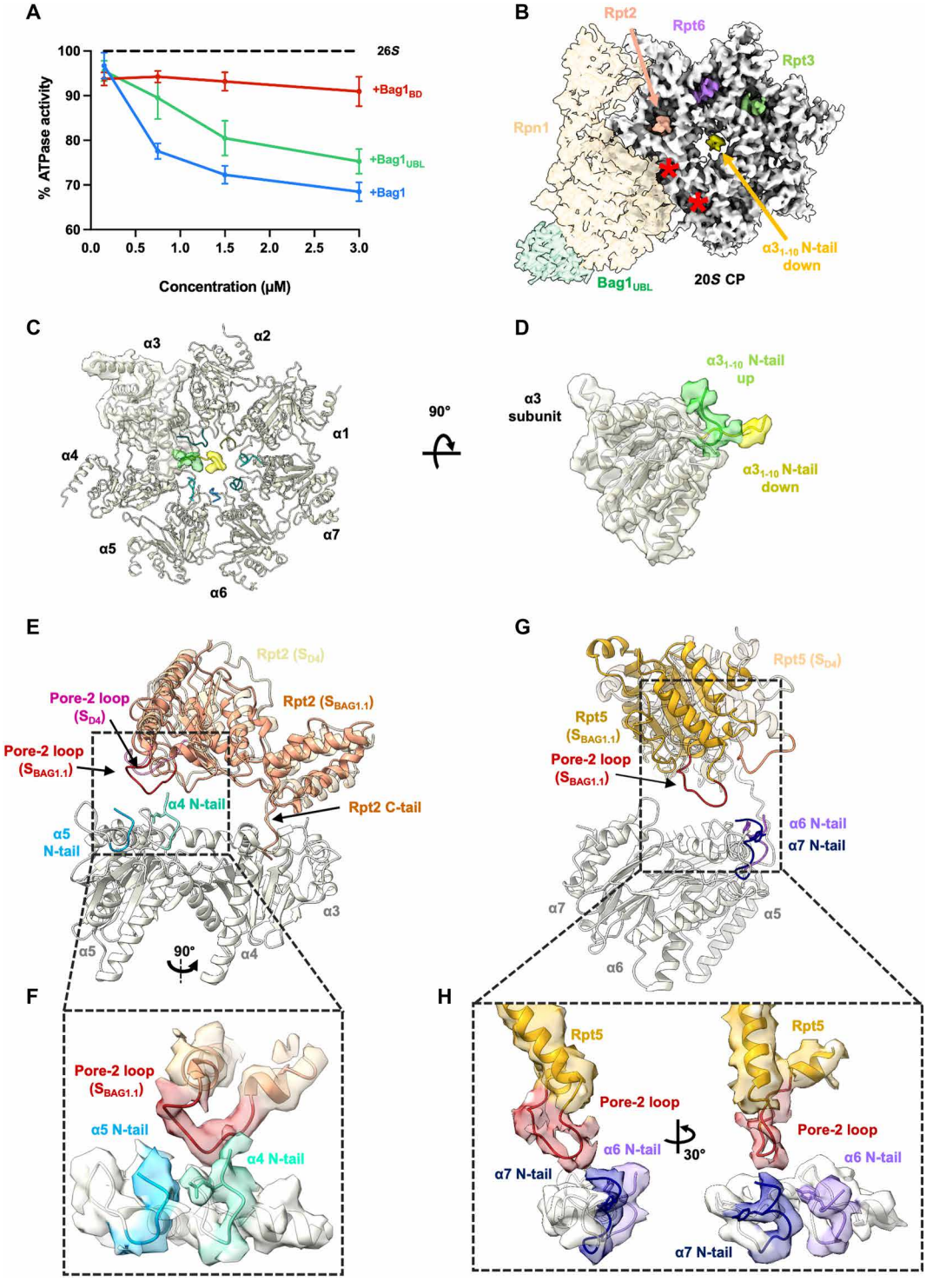

Fig. 5. CP gate–opening mechanism in the Bag1-bound 26*S* proteasome. (**A**) ATPase activity of the 26*S* proteasome (black dashed line) upon Bag1 (blue) $Bag1_{BD}$ (red) or $Bag1_{UBL}$ (green) titration. Whereas $Bag1_{BD}$ shows no effect, full-length Bag1 and $Bag1_{UBL}$ decrease 26*S* ATPase activity. The data represent the means ± SD for $n = 5$ independent experiments (represented with dots). (**B**) The RP-CP interface and insertion of Rpt C-terminal tail into the α pockets of the CP in $S_{BAG1.1}$ are shown. The cryo-EM density of the CP is shown in white, whereas the C-terminal tails of Rpt2, Rpt3, and Rpt6 are colored in salmon, green, and purple, respectively. Empty pockets are indicated with red asterisks. The EM density of the N-terminal tail of α3 in the "down" state is shown in yellow. (**C** and **D**) N-terminal tail of α3 exhibits "up" and "down" states. The "up" conformation (light green) corresponds to the "open" gate, while the "down" conformation (yellow) represents the "closed" gate. Side view of the α3 subunit highlights the movement of the N-terminal tail (D). (**E**) The pore-2 loop of Rpt2 moves lower toward the CP gate, by ~2 Å, and interacts with N-terminal tails of α4 and α5. (**F**) Detailed view of the cryo-EM density of the Rpt2 pore-2 loop and the N-terminal tails of α4 and α5. (**G**) The pore-2 loop of Rpt5 moves lower toward the CP gate, by ~4 Å, and interacts with N-terminal tails of α6 and α7. (**H**) Detailed view of the Rpt5 pore-2 loop and the N-terminal tails of α6 and α7. In (E) and (G), the S_{D4} (PDB: 7W3K) structure was used for comparison of each Rpt subunit.

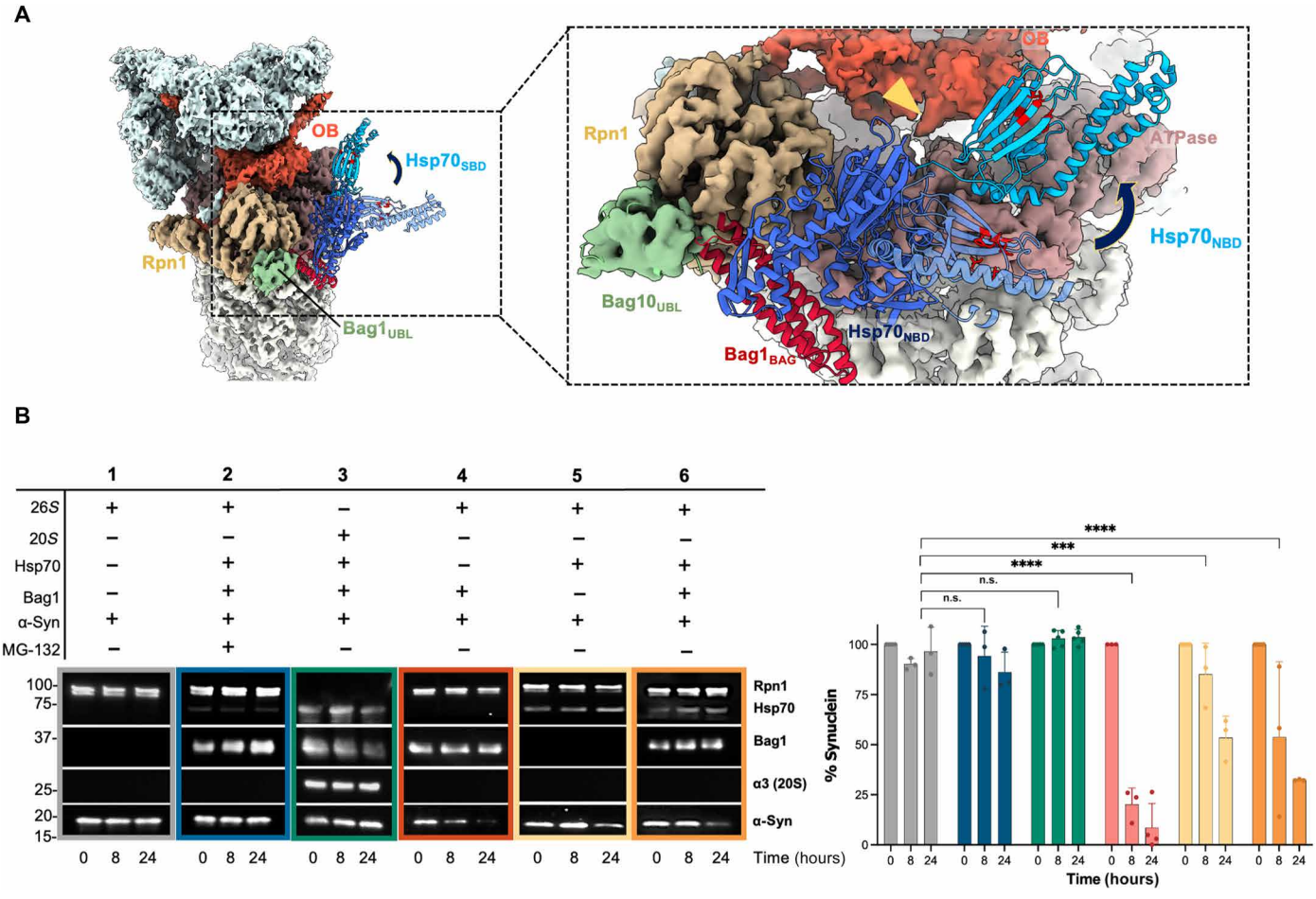

Fig. 6. Structural basis for the unfolded protein transfer. (**A**) Structural model of the Hsp70-Bag1–bound 26*S* proteasome. The $Hsp70_{NBD}$-Bag1 model derived from our ternary complex structure (Fig. 1D) was positioned by aligning $Bag1_{UBL}$ with the $S_{BAG1.1}$ structure. Predicted ADP-bound Hsp70 (AlphaFold) and *E. coli* Hsp70 (PDB: 2KHO) structures are placed by fitting the $Hsp70_{NBD}$. Due to the flexible linker connecting the SBD and NBD, the $Hsp70_{SBD}$ can adopt multiple orientations, potentially facilitating the transfer of unfolded proteins to the proteasome. The substrate binding site of $Hsp70_{SBD}$ is highlighted in red. A large opening between OB and ATPase rings is indicated by a yellow arrowhead. The $Hsp70_{SBD}$ can be positioned adjacent to the OB-ATPase cleft, suggesting a direct route for substrate delivery of unfolded proteins to the proteasome. The Bag1-26*S* proteasome cryo-EM density is presented as a segmented surface (lid, light blue; OB ring, orange; ATPase ring, rosy pink; Rpn1, beige; $Bag1_{UBL}$, light green; and 20*S*, white). The docked $Bag1_{BD}$ (red), $Hsp70_{NBD}$ (blue), and $Hsp70_{SBD}$ (light blue) are shown as a ribbon model. (**B**) Summary of Western blot results (left) analyzing proteasomal degradation of α-syn in the absence of ATP at 0, 8, and 24 hours. Either the 26*S* proteasome or the 20*S* CP was used for the assays. Statistical analysis (right) reveals that Bag1 alone (red) and with Hsp70 (orange) significantly enhance synuclein degradation compared with the proteasome alone (gray), while Hsp70 alone (yellow) shows stronger effects at later time points. MG-132, as expected, inhibits degradation (dark blue). Degradation of α-syn by 20*S* CP was not observed in the presence of Hsp70 and Bag1 (dark green). Data ($n = 4$ to 5) analyzed via two-way analysis of variance (ANOVA; ***$P = 0.0007$; ****$P < 0.0001$). n.s., not significant.

DISCUSSION

In this work, we elucidate the structures of the Bag1-bound 26*S* proteasome, which exhibit notable differences from previously reported proteasome structures (*6*, *7*, *34*, *37*, *38*, *42*). Bag1 binding markedly alters the conformational landscape of the 26*S* proteasome and induces ATPase ring rearrangements distinct from any known AAA^+ ATPase structures (*8*). Similar to observations of the proteasome in complex other UBL-containing cofactors (*18*, *28*, *33*, *34*), Bag1 docks at the T2 site of Rpn1 through the conserved $Bag1_{UBL}$ (Fig. 1, D and E; and fig. S10, A and B), potentially excluding the other cofactors such as Usp14, Rad23, and Dsk2 Ubqln, which are required for Ub-dependent degradation. Although the $Bag1_{BD}$ density was not observed due to the Rpn1 fluctuation, Bag1 binding reorients the Rpt2 N terminus from the $Rpn1_{TD}$ toward its own interface between OB and ATPase domains, enlarging this interdomain contact (fig. S11). This conformational shift repositions Rpn1 toward Rpt2, promoting major structural deformation within the ATPase ring and resulting in the formation of a large central cavity above the open CP gate (Fig. 4A and movie S2).

In canonical ATP-dependent degradation, the pore loops lining the central channel of the AAA^+ ATPases normally make direct contact with the substrate polypeptides with pore-2 loops forming a spiral staircase beneath the pore-1 loops (*6*, *7*, *34*). In contrast, in the Bag1-bound proteasome structures, the pore-2 loops of Rpt2 and Rpt5 contribute to 20*S* gate opening together with the C-terminal tails of Rpt2, Rpt3, and Rpt6 (Fig. 5 and movies S3 and S4), providing insights into a an alternative role of the pore-2 loops. This arrangement is reminiscent of the mitochondrial AAA^+ protease AFG3L2 as its pore-2 loop at the bottom of the staircase contacts the central cavity of the proteolytic chamber to facilitate substrate transfer (*43*). While the three S_{BAG1} structures adopt an open-gate conformation,

the S_{BAG2} subclasses exhibit heterogeneous gate-opening states together with the elevated Rpn1 dynamics, suggesting that S_{BAG2} particles are energetically unstable intermediates, transitioning toward the stable S_{BAG1} structure.

Cooperation with a certain set of co-chaperones enables linking of the Hsp70 chaperones to the 26*S* proteasome for degradation of unfolded proteins (*2*). By combining our cryo-EM structures of the $Hsp70_{NBD}$:Bag1:Rpn1complex and the Bag1-bound 26*S* proteasome, we construct a docking model of the Hsp70:Bag1:26*S* proteasome complex (Fig. 6A). This docking model, supported by XL-MS data, indicates that the $Hsp70_{NBD}$ is positioned near the $Rpn1_{TD}$. Given the flexible linker between NBD and SBD, which allows conformational change upon client or nucleotide binding (*2*), the $Hsp70_{SBD}$ could localize near the expanded interface between the OB and ATPase rings, connecting to the open CP gate for direct substrate transfer.

ATPase activity is impaired in the presence of Bag1 likely due to disruption of the nucleotide-binding interfaces. The modest inhibition by Bag1 may result from its transient interaction. In addition, the observed ATPase activity in the assay could arise from the Bag1-free S_A population, which comprise 23% of the Bag1:26*S* dataset, and from hidden conformations that could not be dissected (fig. S5). Although Hsp70 is thought to assist substrate transfer in an ATP-dependent manner, canonical hand-over-hand translocation by the proteasome ATPase ring is no longer feasible due to the deformation. We therefore propose that the deformed ATPase ring allows direct degradation of unfolded proteins by the 26*S* proteasome in a Ub-independent manner and likely without ATPase motor function (movie S6). Efficient substrate degradation was observed in the presence of Bag1 alone compared to when both Hsp70 and Bag1 are present. On one hand, Hsp70 prevents aggregation of α-syn, which would, otherwise, impair proteasome catalytic activity (*40*). On the other hand, $Hsp70_{SBD}$ may occlude the OB-ATPase opening, thereby preventing nonspecific protein degradation. Considering that Bag1 has a higher affinity for Hsp70 than for Rpn1, a mechanism probably exists whereby only client-bound Hsp70/Bag1complexes are recruited to the 26*S* proteasome. However, further work is needed to clarify the roles of ATP hydrolysis and Hsp70 in this pathway.

Furthermore, the co-chaperone carboxy-terminus of Hsp70-interacting protein (CHIP) E3 ligase interacts with $Hsp70_{SBD}$ and ubiquitinates the Hsp70-bound client proteins (*44*–*46*). The ubiquitinated client is recruited to the proteasome through their polyubiquitin chain (*46*). Because Bag1 can either promote or inhibit CHIP-dependent degradation depending on the substrates (*47*, *48*), the structural mechanisms underlying Bag1/CHIP cooperation, including potential involvement of DUBs, remain to be elucidated.

Recent studies have shown that a subset of eukaryotic proteins is subjected to Ub-independent proteasomal degradation (*12*–*15*, *17*, *49*). Proteomics analysis and global protein stability assay identified nearly 2000 proteins that are degraded by Ub-independent proteasomal degradation, with some of these proteins specifically targeted only under stress conditions (*13*, *16*). Many adaptor proteins such as midnolin and FAT10 have been shown to assist direct protein degradation (*16, 18*), and Bag1:Hsp70 complex appears to facilitate a similar mechanism independently of ubiquitination, as we demonstrated in this study.

Bag1 plays a critical role in maintaining cellular homeostasis under stress conditions, where a rapid cellular response is likely required to prevent protein aggregation (*27*, *50*, *51*). It has been reported that Bag1 protects neuronal cells from the toxicity of various amyloid proteins including α-syn (*52*–*55*). Besides, Hsp70 interacts with IDPs even in the absence of ATP, preventing the amyloid formation (*56*–*58*). It is tempting to speculate that in stress conditions, Bag1 could be upregulated similarly to what occurs with Hsp70, to facilitate the removal of unfolded proteins including amyloid-forming proteins, without the need of Ub tagging. Together, this study describes a previously unidentified mechanism of proteasomal degradation, which not only advances our understanding of the mechanical function of the 26*S* proteasome but also opens new avenues for therapeutic intervention in diseases associated with protein misfolding and aggregation.

MATERIALS AND METHODS

Cloning, expression, and purification of proteins

Human *Rpn1*, *Rpn10*, and *Rpn13* genes were amplified from the cDNA library Human MTC Panel I (Clontech) and cloned into pPROEX-HTa vectors using In-Fusion technique (Takara). Deletion mutants, $Hsp70_{NBD}$, Rpn1ΔNTD, $Bag1_{UBL}$, and $Bag1_{BD}$ were created by subcloning of the targeted genes and cloned into the pPROEX-HTa vector. Proteins were expressed in *E. coli* Rosetta (Rpn1) or C41 strain (Rpn10 and Rpn13). Expression was induced with 1 mM isopropyl-β-D-thiogalactopyranoside at the exponential phase (Rpn10) or using AutoInducible Medium (Rpn1 and Rpn13) (CondaLab). To purify these proteins, cellular lysates were loaded onto HisTrap columns (Cytiva). After tobacco etch virus protease cleavage, to remove the His_6 tag, proteins were further purified by a Q column (Cytiva) and SEC (Superdex 200/75), and the resulting samples were stored at −80°C in 20 mM Hepes (pH 7.4), 150 mM KCl, and 10% glycerol.

Bag1 and Hsp70 were purified, as previously described (*59*). All deletion mutants—$Hsp70_{NBD}$, Rpn1ΔNTD, $Bag1_{UBL}$, and $Bag1_{BD}$—were purified following the same procedure used for their respective full-length proteins. RCMLA was provided by F. Moro (Universidad del País Vasco, Spain). Either human embryonic kidney (HEK) 293T cells (purchased from the Helmholtz Center for Infection Research, Brunswick, Germany) or Expi293F cells (from the Netherlands Cancer Institute, Amsterdam, The Netherlands) were used for proteasome purification, as described in (*60*). Briefly, ~18 g of cells were resuspended in 18 ml of 2× proteasome lysis buffer [100 mM Hepes (pH 7.6), 10 mM dithiothreitol (DTT), 20 mM $MgCl_2$, 10 mM ATP, and 20% (v/v) glycerol], subsequently lysed, and centrifuged at 20,000 rpm for 20 min at 4°C in an SS-34 rotor. The lysate was incubated with 3 μM glutathione *S*-transferase fusion $Rad23_{UBL}$ and 1 ml of Glutathione Sepharose 4B (Cytiva) for 3 hours at 4°C. After washing with proteasome lysis buffer, proteasomes were eluted with the same buffer supplemented with HIS_5-UIM protein (5 mg/ml). The eluted sample was applied to a 15 to 30% (w/v) sucrose gradient [50 mM Hepes (pH 7.6), 50 mM KCl, 5 mM DTT, 10 mM $MgCl_2$, and 7.5 mM ATP]. The gradients were centrifuged at 33,000 rpm for 17 hours at 4°C in an SW40 rotor. Fractions showing peptidase activity were collected and flash frozen in liquid nitrogen and stored at −80°C.

For XL-MS analysis, the ATPase complex was purified from *Saccharomyces cerevisiae*, following a protocol modified from Saeki *et al.* (*61*). *S. cerevisiae* cells (YYS39: *MATa RPN1-3XFLAG::HIS3*) were grown for 72 hours and harvested. The 3XFLAG-tagged 26*S* proteasome was isolated using M2 anti-FLAG beads (Sigma-Aldrich, A2220). The complex was incubated with high-salt buffer [50 mM tris-HCl (pH 7.5), 1.0 M NaCl, and 10% glycerol] to dissociate the 20*S* CP and lid subcomplexes and then washed by the purification buffer [50 mM tris-HCl (pH 7.5), 0.15 M NaCl, and 10% glycerol]. The base complex was eluted by FLAG peptides, and the elution was subjected to a sucrose

gradient (15 to 40%). Fractions containing the ATPase ring but lacking Rpn1 and Rpn2 were identified by SDS–polyacrylamide gel electrophoresis (PAGE) analysis. For degradation assays, the 20*S* CP was purified from discarded human erythrocytes by a combination of ion exchange, hydroxyapatite, and SEC, exactly as described previously (*62*).

Binding assays and SEC analysis

Protein mixtures (10 μM Rpn1/Rpn10/Rpn13, 10 μM Hsp70, and 5 μM Bag1, 2:2:1 molar ratio) were incubated for 20 min at 37°C in a buffer containing 20 mM Hepes (pH 7.4), 150 mM KCl, and 1 mM DTT. The samples were analyzed by SEC using either a Superdex 75 Increase 10/300 GL (Cytiva) or a Superdex 200 10/300 GL (Cytiva), depending on the complex size. The eluted fractions were further analyzed by SDS-PAGE. For the experiment with the quaternary complex, Hsp70 and RCMLA (1 and 4 μM, respectively) were first incubated for 1 hour at 37°C. Bag1 (1 μM) and Rpn1 (1 μM) were then added and incubated for another 20 min at room temperature. The sample was injected into the SEC column, and the obtained fractions were analyzed by SDS-PAGE.

ITC experiments

Proteins were exhaustively dialyzed against 20 mM phosphate buffer (pH 7.4) and 150 mM KCl. The final protein concentration was measured by ultraviolet spectroscopy using the theoretical absorption coefficients at 280 nm (Abs_{280}). ITC experiments were performed at 25°C using a MicroCal PEAQ-ITC microcalorimeter (Malvern). Titrations were performed by stepwise injections of a 100 to 150 μM Bag1 solution into the reaction cell loaded with the other protein/s (16 μM $Hsp70_{NBD}$, Rpn1, or both). Dilution heats were determined separately and subtracted from the total heat produced following each injection. Titration data were analyzed using the AFFINImeter-ITC software. For binary complexes, the data were fitted to a one-site binding model. For the ternary complex, independent binding of Rpn1 and $Hsp70_{NBD}$ was assumed, and data were fitted simultaneously with binary complexes using the same binding parameters for each ligand across both complexes.

XL-MS analysis

For the ternary complex, 10 μM Rpn1, 10 μM Hsp70, and 5 μM Bag1 were incubated together. For the heterobase-Bag1 complex, the isolated ATPase ring (10 μM), Rpn1 (10 μM), Hsp70 (10 μM), and Bag1 (5 μM) were incubated 20 min at 37°C. Both samples were subsequently cross-linked with 3 mM BS3 (Thermo Fisher Scientific) in 20 mM Hepes (pH 7.4), 150 mM KCl, and 1 mM DTT (1 hour, 4°C), followed by quenching with 50 mM tris (pH 7.4). BS3-cross-linked samples were incubated in Laemmli sample buffer for 5 min at 95°C and subjected to SDS-PAGE. The gel was stained with Quick Coomassie (Generon), and the bands corresponding to the complex were excised and subjected to automated reduction with Tris (2 carboxyethyl) phosphine, alkylation with chloroacetamide, and trypsin digestion using an OT2 robot (Opentrons), as described by Shevchenko *et al.* (*63*). The resulting peptide mixture was speed-vac dried and redissolved in 0.1% formic acid for liquid chromatography–tandem mass spectrometry (MS/MS) analysis by Ultimate 3000 nanoHPLC (Dionex) coupled to an Orbitrap Eclipse (Thermo Fisher Scientific) or to an Orbitrap Fusion Lumos (Thermo Fisher Scientific). The high-performance liquid chromatography was equipped with a PepMap Neo C18 trapping column (300 μm by 5 mm; Thermo Fisher Scientific) and a PepMap RSLC c18 column (75 μm by 50 cm; Thermo Fisher Scientific). Solvent A and Solvent B were 0.1% formic acid in water and 0.1% formic acid in acetonitrile, respectively. Separation was performed at 50°C at a flow rate of 250 nl/min under the following gradient: 4% B for 2 min, linear increase to 35% B in 68 min, linear increase to 50% B in 6 min, and linear increase to 90% B in 4 min and 90% B for 10 min.

The mass spectrometer was operated in data-dependent acquisition mode. Each acquisition cycle had a maximum duration of 3 s and consisted of a survey scan (375 to 1250 mass/charge ratio) at 120,000 resolution [full width at half maximum (FWHM)] and up to 20 MS/MS scans at 30,000 resolution (FWHM). Peptides with charges 2 to 6 were selected for fragmentation applying a dynamic exclusion window of 40 s. For peptide identification, raw MS data were converted to mgf files with Proteome Discoverer v2.5 (Thermo Fisher Scientific) that were used for a database search with MeroX 2.0 MeroX 2.0 (*64*) against a custom-made database containing the sequences of each protein. Search parameters were set as follows: trypsin as enzyme allowing two (K) and two (R) missed cleavages, BS3 as cross-linker, MS tolerance of 10 parts per million (ppm) and MS/MS tolerance of 20 ppm, carbamidomethylation of cysteines as fixed modification, and oxidation of methionines as variable modification. Peptide identifications were filtered at a false discovery rate (FDR) of <5% and a minimum MeroX score of 30. Alternatively, the database search was conducted with XlinkX (Thermo Fisher Scientific) with the same database and search parameters except for the number of missed cleavages that was set to 3, and the FDR threshold was <1%. Although conventional constraint distances allowed by BS3 are up to 25 Å (*65*), a broader range (up to 35 Å) was applied to account for protein dynamics and conformational flexibility. The distances that fall within the BS3 constraints established in this work were displayed and represented using Chimera package (*66*).

Proteasome activity

The chymotrypsin 20*S* activity was assayed using the model substrate succinyl- Leu-Leu-Val-Tyr-7-amino-4-methylcoumarin (Suc-LLVY-AMC) (Enzo). A 5 nM concentration of proteasome was preincubated with Bag1 (concentration range from 0.01 μM to 3 μM) for 20 min at 37°C in peptidase buffer [50 mM tris (pH 7.4), 100 mM KCl, 1 mM ATP, 0.5 mM $MgCl_2$, 1 mM DTT, and bovine serum albumin (0.025 mg/ml)], and, later, the Suc-LLVY-AMC substrate (10 μM) was added. The fluorescence was immediately recorded at 37°C using 350-nm excitation and 450-nm emission wavelengths every minute for 1 hour in a SpectraMax ID3 Microplate reader (Molecular Devices). For representation, dots correspond to the mean values of four independent replicates ($n = 4$), and lines correspond to the linear fit of the data for each condition.

ATPase activity assays

These assays were conducted following the standard protocol of BIOMOL GREEN Kit (Enzo). A constant final concentration of 150 nM proteasome was used for the samples when titrating Bag1 with molar ratios of 1:1, 1:5, 1:10, and 1:20. Proteins were mixed in ATPase buffer [20 mM Hepes (pH 7.4), 40 mM NaCl, and 5 mM $MgCl_2$] for a final volume of 25 μl and incubated for 15 min at 37°C with 25 μl of substrate buffer [20 mM tris (pH 7.5), 5 mM $MgCl_2$, and 1 mM ATP]. Then, the reaction was stopped with 100 μl of BIOMOL GREEN reagent and incubated 20 to 30 min at 37°C to allow development of the green color, and the absorbance at 620 nm was measured.

Substrate degradation assays

Reaction mixtures of 350 nM proteasome (26*S* or 20*S*) were incubated in the presence of Bag1 (1.4 μM), Hsp70 (1.4 μM), Hsp40 (1.4 μM), α-syn (0.35 μM), and MG-132 (50 μM). Samples were incubated at room temperature, and 5 μl was collected at 0, 8, and 24 hours. Reactions were stopped by boiling at 95°C for 5 min with SDS-PAGE loading buffer. The samples were loaded onto 4 to 15% Mini-Protean precast gels (Bio-Rad) for SDS-PAGE. Protein bands were transferred to a polyvinylidene difluoride membrane (Immobilon-P transfer membrane from Merck Millipore) using a semidry transfer system (Trans-Blot Turbo from Bio-Rad) at 25 V and 1.0 A for 30 min. Membranes were blocked with 3% (w/v) nonfat dried milk in phosphate-buffered saline containing 0.05% Tween for 1 hour at room temperature, followed by incubation with primary antibodies against Rpn1 (PSMD2 A11, Santa Cruz Biotechnology, 1:300 dilution), $Hsp70_{NBD}$ (501043, PALEX; 1:1000 dilution), Bag1 [α-histidine tag coupled to horseradish peroxidase (HRP), Santa Cruz Biotechnology, 1:4000 dilution], 20*S* (PSMA3; ab109532, Abcam; 1:500 dilution) and α-syn–HRP (Santa Cruz Biotechnology, 1:100 dilution), for 1 hour at room temperature. After incubation with secondary antibody, membranes were developed using Clarity Western ECL substrate (Bio-Rad). The signal of the chemiluminescent bands was analyzed with Fiji, and the obtained data ($n = 4$ to 5) were analyzed via two-way analysis of variance (ANOVA; $^{***}P = 0.0007$; $^{****}P < 0.0001$).

Cryo-EM data acquisition

For the cryo-EM grids of the Bag1:26*S* complex and the other control samples, 1.0 μM 26*S* proteasome and 30 μM Bag1 or Bag1 mutants were incubated together and subsequently cross-linked with 3 mM BS3 (Thermo Fisher Scientific) in 20 mM Hepes (pH 7.4), 150 mM KCl, and 1 mM DTT (1 hour, 4°C), followed by quenching with 50 mM tris (pH 7.4). Aliquots of the 26*S*:Bag1 complex were vitrified in a Vitrobot Mark IV (Thermo Fisher Scientific) at 4°C with 100% humidity. Quantifoil Cu/Rh R2/2 300 mesh grids pretreated with poly-L-lysine (Sigma-Aldrich) were used. Grids without glow discharge were incubated for 90 s with 0.1% poly-L-lysine (w/v), then washed with water, and dried (*67*). A total of 14,079 images were acquired in a Titan Krios (Thermo Fisher Scientific) equipped with a K3 detector (Gatan Inc.). A total dose of 37 electron (e^-)/Å^2 was applied to the images with nominal defocus ranged from −1 to −3 μm. The magnification was ×81,000, corresponding to a pixel size of 1.06 Å.

Three control samples, namely, 26*S*:$Bag1_{BD}$, 26*S*:$Bag1_{UBL}$, and 26*S*:BS3, prepared in the same manner with the 26*S*:Bag1 sample, were vitrified in a Vitrobot Mark IV (Thermo Fisher Scientific). Three microliters of the samples were applied to freshly glow discharged Quantifoil Cu R2/2 200 mesh grids, washed with water, and blotted. A total of 6685, 5051, and 5887 images were acquired for the control samples, respectively, in a Titan Krios (Thermo Fisher Scientific) equipped with a Selectris energy filter operating at a slit width of 10 eV and Falcon4i detector (Thermo Fisher Scientific). The magnification was ×105,000, corresponding to a pixel size of 1.18 Å. A total dose of 40 e^-/Å^2 was applied to the images with nominal defocus range from −1 to −2 μm.

For the Rpn1:Bag1:$Hsp70_{NBD}$ complex, 10 μM Rpn1, 10 μM $Hsp70_{NBD}$, and 5 μM Bag1 (2:2:1 molar ratio) were incubated for 20 min at 37°C. Cross-linking was carried out using 1 mM BS3 for 1 hour at 4°C, and the reaction was quenched with 50 mM tris (pH 7.4). All three proteins were individually purified before complex formation, as detailed in the "Cloning, expression and purification of proteins" section. Additionally, the sample was subjected to SEC using a Superdex 200 10/300 GL (Cytiva) column to isolate the ternary complex. Subsequently, aliquots of the complex were vitrified in a Vitrobot Mark IV (Thermo Fisher Scientific) at 4°C with 100% humidity. Glow-discharged UltrAuFoil R1.2/1.3 300 mesh grids were used. A total of 13,724 images were acquired in a Titan Krios (Thermo Fisher Scientific) equipped with a K3 detector (Gatan Inc.). A total dose of 42 e^-/Å^2 was applied to the images with nominal defocus range from −1.4 to −3 μm and a magnification of ×81,000, corresponding to a pixel size of 1.06 Å. Details of the data acquisitions are provided in table S3.

Image processing and 3D reconstruction

Initial preprocessing of the 26*S*:Bag1 complex data, including movie frame alignment by MotionCorr2 (*68*), contrast transfer function (CTF) estimation by CTFFIND4 (*69*), and cleaning up of particles were performed using the Scipion 3.0 software platform (*70*). A total of 1,891,841 particles were picked by crYOLO (*71*). A total of 605,539 particles were identified after rounds of CryoSPARC 2D classifications, and, hereafter, image processing was performed on Relion (*72*) or CryoSPARC (*73*). A further Relion 4.0 2D classification reduced the number of good particles to 542,965, which was then subjected to a Relion 4.0 3D classification as well as cryoDRGN analysis (*35*) to investigate the conformational landscape of the samples. It identified a distinct subset of particles that eventually led to a 3.2-Å reconstruction (Conformation 3, similar to S_A) with 104,849 particles using Relion 4.0 AutoRefine. The rest of the particles were then imported to CryoSPARC for 3D classification. It captured a distinct class of 26*S* proteasome where the ATPase ring largely expanded (57,564 particles), as well as three classes of 26*S* proteasome with different degrees of ATPase ring expansion and extensive Rpn1 flexibilities (254,363 particles). Further 3D classification on the set of 57,564 particles identified three variations of the substantial ATPase expansion, namely, $S_{BAG1.1}$ (21,831 particles, 3.6-Å resolution), $S_{BAG1.2}$ (16,466 particles, 3.5-Å resolution), and $S_{BAG1.3}$ (19,267 particles, 3.6-Å resolution) using nonuniform refinement in CryoSPARC. To better resolve densities around the expanded ATPase, a local refine in CryoSPARC was performed on $S_{BAG1.1}$ particles, leading to a map with slightly lower global Fourier shell correlation (3.7 Å) but better resolved local densities around ATPase. Further focused 3D classifications of the set of 254,363 particles in Relion 5.0 led to the identification of a conformation with better resolved Rpn1 and expanded ATPase densities, named S_{BAG2} (59,907 particles, 3.7-Å resolution).

For the control datasets 26*S*:$Bag1_{UBL}$, 26*S*:$Bag1_{BD}$, and 26*S*:BS3, movie frame alignment was performed using cryoSPARC, followed by CTF estimation by CTFFIND4. A total of 602,653, 648,687, and 712,653 particles were initially picked by crYOLO for 26*S*:$Bag1_{UBL}$, 26*S*:$Bag1_{BD}$, and 26*S*:BS3 datasets, respectively. After multiple rounds of 2D classification and 3D classification in Relion 4.0, followed by cryoDRGN analysis (*35*) to investigate the conformational landscape of the samples. No map with expanded ATPase ring like S_{BAG} could be found in these three datasets.

Initial movie frame alignment and CTF estimation of the $Hsp70_{NBD}$:Rpn1:Bag1 complex were performed using cryoSPARC. A total of 6,415,119 particles were picked by crYOLO using a network trained on a subset of the datasets. After multiple rounds of 2D classification, 743,645 particles were subjected to Ab Initio Reconstruction in CryoSPARC with five classes. A good class was selected for further processing, which corresponded to 223,163 particles. It was subjected to

Relion 5.0 focused refinement, followed by particle subtraction, focused refinement, and focused classification; two conformations of the ternary complex of the $Hsp70_{NBD}$:Bag1:Rpn1 can be identified (25,238 particles, 4.8-Å resolution; and 30,256 particles, 6.2-Å resolution).

Model building

For the Bag1-bound 26*S* proteasome, the model was built on $S_{BAG1.1}$ map. The published model (PDB ID: 7W3K) was used as initial reference. Most of the chains fit into the densities readily, whereas the ATPase chains were individually docked to the corresponding densities, followed by multiple rounds of manual adjustment in Coot (*74*) and real-space refinement in PHENIX (*75*). The $S_{BAG1.1}$ model was then used to build models on $S_{BAG1.2}$ map and $S_{BAG1.3}$ map. It began with global rigid body fitting of $S_{BAG1.1}$ model into the maps, followed by rigid body fitting on each ATPase chains. The models were then adjusted manually in Coot, followed by real-space refinement in PHENIX. Details of the model-building process and the quality of the final atomic models are provided in table S4.

The current model and 7w3k were aligned on the 20*S* for root mean square deviation (RMSD) measurement of the Rpt subunits. Per-residue RMSD measurement on the main chain of the ATPase domain was calculated on the basis of BioPandas (*76*). The script is available on Zenodo (17424377).

Supplementary Materials

The PDF file includes:

Figs. S1 to S16
Tables S1 to S4
Legends for movies S1 to S6

Other Supplementary Material for this manuscript includes the following:

Movies S1 to S6

REFERENCES

1. B. Chen, M. Retzlaff, T. Roos, J. Frydman, Cellular strategies of protein quality control. *Cold Spring Harb. Perspect. Biol.* **3**, a004374 (2011).
2. R. Rosenzweig, N. B. Nillegoda, M. P. Mayer, B. Bukau, The Hsp70 chaperone network. *Nat. Rev. Mol. Cell Biol.* **20**, 665–680 (2019).
3. M. S. Hipp, S. H. Park, F. U. Hartl, Proteostasis impairment in protein-misfolding and -aggregation diseases. *Trends Cell Biol.* **24**, 506–514 (2014).
4. R. J. Tomko Jr., M. Hochstrasser, Molecular architecture and assembly of the eukaryotic proteasome. *Annu. Rev. Biochem.* **82**, 415–445 (2013).
5. D. Finley, Recognition and processing of ubiquitin-protein conjugates by the proteasome. *Annu. Rev. Biochem.* **78**, 477–513 (2009).
6. A. H. de la Peña, E. A. Goodall, S. N. Gates, G. C. Lander, A. Martin, Substrate-engaged 26*S* proteasome structures reveal mechanisms for ATP-hydrolysis-driven translocation. *Science* **362**, eaav0725 (2018).
7. Y. Dong, S. Zhang, Z. Wu, X. Li, W. L. Wang, Y. Zhu, S. Stoilova-McPhie, Y. Lu, D. Finley, Y. Mao, Cryo-EM structures and dynamics of substrate-engaged human 26S proteasome. *Nature* **565**, 49–55 (2019).
8. C. Puchades, C. R. Sandate, G. C. Lander, The molecular principles governing the activity and functional diversity of AAA+ proteins. *Nat. Rev. Mol. Cell Biol.* **21**, 43–58 (2020).
9. S. Elsasser, R. R. Gali, M. Schwickart, C. N. Larsen, D. S. Leggett, B. Muller, M. T. Feng, F. Tubing, G. A. Dittmar, D. Finley, Proteasome subunit Rpn1 binds ubiquitin-like protein domains. *Nat. Cell Biol.* **4**, 725–730 (2002).
10. J. Hanna, N. A. Hathaway, Y. Tone, B. Crosas, S. Elsasser, D. S. Kirkpatrick, D. S. Leggett, S. P. Gygi, R. W. King, D. Finley, Deubiquitinating enzyme Ubp6 functions noncatalytically to delay proteasomal degradation. *Cell* **127**, 99–111 (2006).
11. J. Lüders, J. Demand, J. Höhfeld, The ubiquitin-related BAG-1 provides a link between the molecular chaperones Hsc70/Hsp70 and the proteasome. *J. Biol. Chem.* **275**, 4613–4617 (2000).
12. G. Kandasamy, C. Andreasson, Hsp70-Hsp110 chaperones deliver ubiquitin-dependent and -independent substrates to the 26S proteasome for proteolysis in yeast. *J. Cell Sci.* **131**, jcs210948 (2018).
13. Y. Makaros, A. Raiff, R. T. Timms, A. R. Wagh, M. I. Gueta, A. Bekturova, J. Guez-Haddad, S. Brodsky, Y. Opatowsky, M. H. Glickman, S. J. Elledge, I. Koren, Ubiquitin-independent proteasomal degradation driven by C-degron pathways. *Mol. Cell* **83**, 1921–1935.e7 (2023).
14. G. K. Tofaris, R. Layfield, M. G. Spillantini, α-Synuclein metabolism and aggregation is linked to ubiquitin-independent degradation by the proteasome. *FEBS Lett.* **509**, 22–26 (2001).
15. T. Grune, D. Botzen, M. Engels, P. Voss, B. Kaiser, T. Jung, S. Grimm, G. Ermak, K. J. Davies, Tau protein degradation is catalyzed by the ATP/ubiquitin-independent 20S proteasome under normal cell conditions. *Arch. Biochem. Biophys.* **500**, 181–188 (2010).
16. X. Gu, C. Nardone, N. Kamitaki, A. Mao, S. J. Elledge, M. E. Greenberg, The midnolin-proteasome pathway catches proteins for ubiquitination-independent degradation. *Science* **381**, eadh5021 (2023).
17. X. Chen, Y. Chi, A. Bloecher, R. Aebersold, B. E. Clurman, J. M. Roberts, N-acetylation and ubiquitin-independent proteasomal degradation of p21(Cip1). *Mol. Cell* **16**, 839–847 (2004).
18. C. Arkinson, K. C. Dong, C. L. Gee, S. M. Costello, A. C. Soe, G. L. Hura, S. Marqusee, A. Martin, NUB1 traps unfolded FAT10 for ubiquitin-independent degradation by the 26S proteasome. *Nat. Struct. Mol. Biol.* **32**, 1752–1765 (2025).
19. A. Bracher, J. Verghese, The nucleotide exchange factors of Hsp70 molecular chaperones. *Front. Mol. Biosci.* **2**, 10 (2015).
20. M. Kabbage, M. B. Dickman, The BAG proteins: A ubiquitous family of chaperone regulators. *Cell. Mol. Life Sci.* **65**, 1390–1402 (2008).
21. S. Takayama, T. Sato, S. Krajewski, K. Kochel, S. Irie, J. A. Millan, J. C. Reed, Cloning and functional analysis of BAG-1: A novel Bcl-2-binding protein with anti-cell death activity. *Cell* **80**, 279–284 (1995).
22. S. Takayama, D. N. Bimston, S. Matsuzawa, B. C. Freeman, C. Aime-Sempe, Z. Xie, R. I. Morimoto, J. C. Reed, BAG-1 modulates the chaperone activity of Hsp70/Hsc70. *EMBO J.* **16**, 4887–4896 (1997).
23. J. Höhfeld, S. Jentsch, GrpE-like regulation of the hsc70 chaperone by the anti-apoptotic protein BAG-1. *EMBO J.* **16**, 6209–6216 (1997).
24. D. A. Knee, B. A. Froesch, U. Nuber, S. Takayama, J. C. Reed, Structure-function analysis of Bag1 proteins. Effects on androgen receptor transcriptional activity. *J. Biol. Chem.* **276**, 12718–12724 (2001).
25. J. Song, M. Takeda, R. I. Morimoto, Bag1-Hsp70 mediates a physiological stress signalling pathway that regulates Raf-1/ERK and cell growth. *Nat. Cell Biol.* **3**, 276–282 (2001).
26. E. Venturelli, C. Villa, C. Fenoglio, F. Clerici, A. Marcone, L. Benussi, R. Ghidoni, S. Gallone, F. Cortini, M. Serpente, C. Cantoni, G. Fumagalli, E. Ridolfi, S. Cappa, G. Binetti, M. Franceschi, I. Rainero, M. T. Giordana, C. Mariani, N. Bresolin, E. Scarpini, D. Galimberti, BAG1 is a protective factor for sporadic frontotemporal lobar degeneration but not for Alzheimer's disease. *J. Alzheimers Dis.* **23**, 701–707 (2011).
27. S. Takayama, S. Krajewski, M. Krajewska, S. Kitada, J. M. Zapata, K. Kochel, D. Knee, D. Scudiero, G. Tudor, G. J. Miller, T. Miyashita, M. Yamada, J. C. Reed, Expression and location of Hsp70/Hsc-binding anti-apoptotic protein BAG-1 and its variants in normal tissues and tumor cell lines. *Cancer Res.* **58**, 3116–3131 (1998).
28. Y. Shi, X. Chen, S. Elsasser, B. B. Stocks, G. Tian, B.-H. Lee, Y. Shi, N. Zhang, S. A. H. de Poot, F. Tuebing, S. Sun, J. Vannoy, S. G. Tarasov, J. R. Engen, D. Finley, K. J. Walters, Rpn1 provides adjacent receptor sites for substrate binding and deubiquitination by the proteasome. *Science* **351**, 10.1126/science.aad9421 (2016).
29. D. R. Palleros, L. Shi, K. L. Reid, A. L. Fink, hsp70-protein complexes. Complex stability and conformation of bound substrate protein. *J. Biol. Chem.* **269**, 13107–13114 (1994).
30. R. Y.-R. Wang, C. M. Noddings, E. Kirschke, A. G. Myasnikov, J. L. Johnson, D. A. Agard, Structure of Hsp90-Hsp70-Hop-GR reveals the Hsp90 client-loading mechanism. *Nature* **601**, 460–464 (2022).
31. H. Sondermann, C. Scheufler, C. Schneider, J. Hohfeld, F. U. Hartl, I. Moarefi, Structure of a Bag/Hsc70 complex: Convergent functional evolution of Hsp70 nucleotide exchange factors. *Science* **291**, 1553–1557 (2001).
32. J. Jumper, R. Evans, A. Pritzel, T. Green, M. Figurnov, O. Ronneberger, K. Tunyasuvunakool, R. Bates, A. Žídek, A. Potapenko, A. Bridgland, C. Meyer, S. A. A. Kohl, A. J. Ballard, A. Cowie, B. Romera-Paredes, S. Nikolov, R. Jain, J. Adler, T. Back, S. Petersen, D. Reiman, E. Clancy, M. Zielinski, M. Steinegger, M. Pacholska, T. Berghammer, S. Bodenstein, D. Silver, O. Vinyals, A. W. Senior, K. Kavukcuoglu, P. Kohli, D. Hassabis, Highly accurate protein structure prediction with AlphaFold. *Nature* **596**, 583–589 (2021).
33. K. Y. S. Hung, S. Klumpe, M. R. Eisele, S. Elsasser, G. Tian, S. Sun, J. A. Moroco, T. C. Cheng, T. Joshi, T. Seibel, D. Van Dalen, X. H. Feng, Y. Lu, H. Ovaa, J. R. Engen, B. H. Lee, T. Rudack, E. Sakata, D. Finley, Allosteric control of Ubp6 and the proteasome via a bidirectional switch. *Nat. Commun.* **13**, 838 (2022).
34. S. Zhang, S. Zou, D. Yin, L. Zhao, D. Finley, Z. Wu, Y. Mao, USP14-regulated allostery of the human proteasome by time-resolved cryo-EM. *Nature* **605**, 567–574 (2022).
35. E. D. Zhong, T. Bepler, B. Berger, J. H. Davis, CryoDRGN: Reconstruction of heterogeneous cryo-EM structures using neural networks. *Nat. Methods* **18**, 176–185 (2021).

36. H. T. Kim, A. L. Goldberg, UBL domain of Usp14 and other proteins stimulates proteasome activities and protein degradation in cells. *Proc Natl Acad Sci U.S.A.* **115**, E11642–E11650 (2018).
37. M. R. Eisele, R. G. Reed, T. Rudack, A. Schweitzer, F. Beck, I. Nagy, G. Pfeifer, J. M. Plitzko, W. Baumeister, R. J. Tomko Jr., E. Sakata, Expanded coverage of the 26S proteasome conformational landscape reveals mechanisms of peptidase gating. *Cell Rep.* **24**, 1301–1315.e5 (2018).
38. S. Chen, J. Wu, Y. Lu, Y. B. Ma, B.-H. Lee, Z. Yu, Q. Ouyang, D. J. Finley, M. W. Kirschner, Y. Mao, Structural basis for dynamic regulation of the human 26S proteasome. *Proc. Natl. Acad. Sci. U.S.A.* **113**, 12991–12996 (2016).
39. P. Calabresi, A. Mechelli, G. Natale, L. Volpicelli-Daley, G. Di Lazzaro, V. Ghiglieri, α-synuclein in Parkinson's disease and other synucleinopathies: From overt neurodegeneration back to early synaptic dysfunction. *Cell Death Dis.* **14**, 176 (2023).
40. T. A. Thibaudeau, R. T. Anderson, D. M. Smith, A common mechanism of proteasome impairment by neurodegenerative disease-associated oligomers. *Nat. Commun.* **9**, 1097 (2018).
41. J. H. Seo, J.-H. Park, E. J. Lee, T. T. Vo, H. Choi, J. Y. Kim, J. K. Jang, H.-J. Wee, H. S. Lee, S. H. Jang, Z. Y. Park, J. Jeong, K.-J. Lee, S.-H. Seok, J. Y. Park, B. J. Lee, M.-N. Lee, G. T. Oh, K.-W. Kim, ARD1-mediated Hsp70 acetylation balances stress-induced protein refolding and degradation. *Nat. Commun.* **7**, 12882 (2016).
42. D. Lee, Y. Zhu, L. Colson, X. Wang, S. Chen, E. Tkacik, L. Huang, Q. Ouyang, A. L. Goldberg, Y. Lu, Molecular mechanism for activation of the 26S proteasome by ZFAND5. *Mol. Cell* **83**, 2959–2975.e7 (2023).
43. C. Puchades, B. Ding, A. Song, R. L. Wiseman, G. C. Lander, S. E. Glynn, Unique structural features of the mitochondrial AAA+ protease AFG3L2 reveal the molecular basis for activity in health and disease. *Mol. Cell* **75**, 1073–1085.e6 (2019).
44. C. A. Ballinger, P. Connell, Y. Wu, Z. Hu, L. J. Thompson, L. Y. Yin, C. Patterson, Identification of CHIP, a novel tetratricopeptide repeat-containing protein that interacts with heat shock proteins and negatively regulates chaperone functions. *Mol. Cell. Biol.* **19**, 4535–4545 (1999).
45. P. Connell, C. A. Ballinger, J. Jiang, Y. Wu, L. J. Thompson, J. Höhfeld, C. Patterson, The co-chaperone CHIP regulates protein triage decisions mediated by heat-shock proteins. *Nat. Cell Biol.* **3**, 93–96 (2001).
46. J. Jiang, C. A. Ballinger, Y. Wu, Q. Dai, D. M. Cyr, J. Höhfeld, C. Patterson, CHIP is a U-box-dependent E3 ubiquitin ligase: Identification of Hsc70 as a target for ubiquitylation. *J. Biol. Chem.* **276**, 42938–42944 (2001).
47. M. Stankiewicz, R. Nikolay, V. Rybin, M. P. Mayer, CHIP participates in protein triage decisions by preferentially ubiquitinating Hsp70-bound substrates. *FEBS J.* **277**, 3353–3367 (2010).
48. Y. Matsumura, L. L. David, W. R. Skach, Role of Hsc70 binding cycle in CFTR folding and endoplasmic reticulum-associated degradation. *Mol. Biol. Cell* **22**, 2797–2809 (2011).
49. D. C. Carrettiero, M. C. Almeida, A. P. Longhini, J. N. Rauch, D. Han, X. Zhang, S. Najafi, J. E. Gestwicki, K. S. Kosik, Stress routes clients to the proteasome via a BAG2 ubiquitin-independent degradation condensate. *Nat. Commun.* **13**, 3074 (2022).
50. R. Götz, S. Wiese, S. Takayama, G. C. Camarero, W. Rossoll, U. Schweizer, J. Troppmair, S. Jablonka, B. Holtmann, J. C. Reed, U. R. Rapp, M. Sendtner, Bag1 is essential for differentiation and survival of hematopoietic and neuronal cells. *Nat. Neurosci.* **8**, 1169–1178 (2005).
51. J. Liman, S. Ganesan, C. P. Dohm, S. Krajewski, J. C. Reed, M. Bähr, F. S. Wouters, P. Kermer, Interaction of BAG1 and Hsp70 mediates neuroprotectivity and increases chaperone activity. *Mol. Cell. Biol.* **25**, 3715–3725 (2005).
52. N. R. Jana, N. Nukina, BAG-1 associates with the polyglutamine-expanded huntingtin aggregates. *Neurosci. lett.* **378**, 171–175 (2005).
53. A. L. Orr, S. Huang, M. A. Roberts, J. C. Reed, S. Li, X.-J. Li, Sex-dependent effect of BAG1 in ameliorating motor deficits of Huntington disease transgenic mice. *J. Biol. Chem* **283**, 16027–16036 (2008).
54. E. Elliott, O. Laufer, I. Ginzburg, BAG-1M is up-regulated in hippocampus of Alzheimer's disease patients and associates with tau and APP proteins. *J. Neurochem.* **109**, 1168–1178 (2009).
55. P. Kermer, A. Köhn, M. Schnieder, P. Lingor, M. Bähr, J. Liman, C. P. Dohm, BAG1 is neuroprotective in in vivo and in vitro models of Parkinson's disease. *J. Mol. Neurosci.* **55**, 587–595 (2015).
56. N. Chilukoti, T. B. Sil, B. Sahoo, S. Deepa, S. Cherakara, M. Maddheshiya, K. Garai, Hsp70 inhibits aggregation of IAPP by binding to the heterogeneous prenucleation oligomers. *Biophys. J.* **120**, 476–488 (2021).
57. P. Fernandez-Funez, J. Sanchez-Garcia, L. de Mena, Y. Zhang, Y. Levites, S. Khare, T. E. Golde, D. E. Rincon-Limas, Holdase activity of secreted Hsp70 masks amyloid-β42 neurotoxicity in *Drosophila*. *Proc. Natl. Acad. Sci. U.S.A.* **113**, E5212–E5221 (2016).
58. A. Franco, J. Cuéllar, J. A. Fernández-Higuero, I. de la Arada, N. Orozco, J. M. Valpuesta, A. Prado, A. Muga, Truncation-driven lateral association of α-synuclein hinders amyloid clearance by the Hsp70-based disaggregase. *Int. J. Mol. Sci.* **22**, 12983 (2021).
59. L. Quintana-Gallardo, J. Martin-Benito, M. Marcilla, G. Espadas, E. Sabidó, J. M. Valpuesta, The cochaperone CHIP marks Hsp70- and Hsp90-bound substrates for degradation through a very flexible mechanism. *Sci. Rep.* **9**, 5102 (2019).
60. H. C. Besche, W. Haas, S. P. Gygi, A. L. Goldberg, Isolation of mammalian 26S proteasomes and p97/VCP complexes using the ubiquitin-like domain from HHR23B reveals novel proteasome-associated proteins. *Biochemistry* **48**, 2538–2549 (2009).
61. Y. Saeki, A. Toh-e, H. Yokosawa, Rapid isolation and characterization of the yeast proteasome regulatory complex. *Biochem. Biophys. Res. Commun.* **273**, 509–515 (2000).
62. M. J. McGuire, M. L. McCullough, D. E. Croall, G. N. DeMartino, The high molecular weight multicatalytic proteinase, macropain, exists in a latent form in human erythrocytes. *Biochim. Biophys. Acta* **995**, 181–186 (1989).
63. A. Shevchenko, M. Wilm, O. Vorm, M. Mann, Mass spectrometric sequencing of proteins silver-stained polyacrylamide gels. *Anal. Chem.* **68**, 850–858 (1996).
64. M. Götze, J. Pettelkau, R. Fritzsche, C. H. Ihling, M. Schäfer, A. Sinz, Automated assignment of MS/MS cleavable cross-links in protein 3D-structure analysis. *J. Am. Soc. Mass Spectrom.* **26**, 83–97 (2015).
65. E. D. Merkley, S. Rysavy, A. Kahraman, R. P. Hafen, V. Daggett, J. N. Adkins, Distance restraints from crosslinking mass spectrometry: Mining a molecular dynamics simulation database to evaluate lysine-lysine distances. *Protein Sci.* **23**, 747–759 (2014).
66. E. C. Meng, T. D. Goddard, E. F. Pettersen, G. S. Couch, Z. J. Pearson, J. H. Morris, T. E. Ferrin, UCSF ChimeraX: Tools for structure building and analysis. *Protein Sci.* **32**, e4792 (2023).
67. J. Cuéllar, W. G. Ludlam, N. C. Tensmeyer, T. Aoba, M. Dhavale, C. Santiago, M. T. Bueno-Carrasco, M. J. Mann, R. L. Plimpton, A. Makaju, S. Franklin, B. M. Willardson, J. M. Valpuesta, Structural and functional analysis of the role of the chaperonin CCT in mTOR complex assembly. *Nat. Commun.* **10**, 2865 (2019).
68. S. Q. Zheng, E. Palovcak, J.-P. Armache, K. A. Verba, Y. Cheng, D. A. Agard, MotionCor2: Anisotropic correction of beam-induced motion for improved cryo-electron microscopy. *Nat. Methods* **14**, 331–332 (2017).
69. A. Rohou, N. Grigorieff, CTFFIND4: Fast and accurate defocus estimation from electron micrographs. *J. Struct. Biol.* **192**, 216–221 (2015).
70. J. M. de la Rosa-Trevín, A. Quintana, L. Del Cano, A. Zaldivar, I. Foche, J. Gutiérrez, J. Gómez-Blanco, J. Burguet-Castell, J. Cuenca-Alba, V. Abrishami, J. Vargas, J. Otón, G. Sharov, J. L. Vilas, J. Navas, P. Conesa, M. Kazemi, R. Marabini, C. O. Sorzano, J. M. Carazo, Scipion: A software framework toward integration, reproducibility and validation in 3D electron microscopy. *J. Struct. Biol.* **195**, 93–99 (2016).
71. T. Wagner, F. Merino, M. Stabrin, T. Moriya, C. Antoni, A. Apelbaum, P. Hagel, O. Sitsel, T. Raisch, D. Prumbaum, D. Quentin, D. Roderer, S. Tacke, B. Siebolds, E. Schubert, T. R. Shaikh, P. Lill, C. Gatsogiannis, S. Raunser, SPHIRE-crYOLO is a fast and accurate fully automated particle picker for cryo-EM. *Commun. Biol.* **2**, 218 (2019).
72. S. H. W. Scheres, RELION: Implementation of a Bayesian approach to cryo-EM structure determination. *J. Struct. Biol.* **180**, 519–530 (2012).
73. A. Punjani, J. L. Rubinstein, D. J. Fleet, M. A. Brubaker, cryoSPARC: Algorithms for rapid unsupervised cryo-EM structure determination. *Nat. Methods* **14**, 290–296 (2017).
74. P. Emsley, B. Lohkamp, W.G. Scott, K. Cowtan, Features and development of Coot. *Acta Crystallogr. D Struct. Biol.* **66**, 486–501 (2010).
75. D. Liebschner, P. V. Afonine, M. L. Baker, G. Bunkóczi, V. B. Chen, T. I. Croll, B. Hintze, L. W. Hung, S. Jain, A. J. McCoy, N. W. Moriarty, R. D. Oeffner, B. K. Poon, M. G. Prisant, R. J. Read, J. S. Richardson, D. C. Richardson, M. D. Sammito, O. V. Sobolev, D. H. Stockwell, T. C. Terwilliger, A. G. Urzhumtsev, L. L. Videau, C. J. Williams, P. D. Adams, Macromolecular structure determination using x-rays, neutrons and electrons: recent developments in phenix. *Acta Crystallogr. D Struct. Biol.* **75**, 861–877 (2019).
76. S. Raschka, BioPandas: Working with molecular structures in pandas DataFrames. *J. Open Source Softw.* **2**, 279 (2017).

Acknowledgments: We thank J. van den Heuvel in the Helmholtz Centre for Infection Research, Germany, and Instruct-ERIC, The Netherlands (PID 26461), for providing biomass of HEK cells. Special thanks to the European Synchrotron Radiation Facility (ESRF) in Grenoble for access to the Titan Krios cryo–electron microscope (MX2263). We acknowledge the technical support of the cryo-EM CNB-CSIC facility. We thank R. Fernández Busnadiego for critical reading of the manuscript. **Funding:** We acknowledge the support of the Spanish State Research Agency through grants PID2022-137175NB-I00 (AEI/FEDER, UE) and AEI/10.13039/501100011033, through the "Severo Ochoa" Programme for Centres of Excellence in R&D (CEX2023-001386-S) to J.M.V. and J.C. The support the grant Caixa Research Health 2023 (HR23-00837 to J.M.V.) is also acknowledged. Support was also provided by the German Research Foundation (DFG) through CRC889 (project number 154113120; project A11 to E.S.), SFB1690 (project A02 to E.S.), Germany's Excellence Strategy (project number EXC 2067/1-390729940 to E.S.), and National Institutes of Health R01GM118600 (to R.J.T.). Cryo-ET instrumentation was jointly funded by the DFG Major Research Instrumentation program and the Ministry of Science and Culture of the State of Lower Saxony (448415290 to E.S.). Additional funding was provided to M.M. by the Centro de Investigación Biomédica en Red de Enfermedades Respiratorias (CIBERES), an initiative of the Instituto de Salud Carlos III (ISCIII). **Author contributions:** Protein samples were produced by M.M.-L., J.M., A.S., M.I., R.J.T., and M.A. M.M.-L., T.C.C., E.S., and J.M. performed and analyzed the cryo-EM experiments. M.M. and M.M.-L. performed and analyzed the ITC experiments. J.M.V., J.C., and E.S. designed and supervised the research. Figures and movies were prepared by J.M., and E.S. E.S., J.C., and J.M.V. wrote the manuscript with contributions from all authors.

Competing interests: The authors declare that they have no competing interests. **Data, code, and materials availability:** All data and code needed to evaluate and reproduce the results in the paper are present in the paper and/or the Supplementary Materials. The cryo-EM reconstructions of the Bag1-bound 26*S* proteasome have been deposited in the Electron microscopy Data Bank (www.emdatabank.org) under the following accession codes EMD-52097 ($S_{BAG1.1}$), EMD-52193 ($S_{BAG1.2}$), EMD-52194 ($S_{BAG1.3}$), and EMD-53945 (S_{BAG2}). The cryo-EM reconstructions of the ternary complex of $Hsp70_{NBD}$:Bag1:Rpn1 are deposited under EMDB accession codes 52195 (class 1) and 52196 (class 2). Atomic model coordinates and associated structure factors of the Bag1-bound 26*S* proteasome are deposited in Protein Data Bank database (www.pdb.org) under PDB accession codes 9HEU ($S_{BAG1.1}$), 9SZT ($S_{BAG1.2}$), and 9SZV ($S_{BAG1.3}$). XL-MS data have been deposited to the ProteomeXchange Consortium via the PRIDE partner repository with the dataset identifiers PXD058407 and PXD069071. The script for residual RMSD measurement is available on Zenodo (https://zenodo.org/records/17424377).

Submitted 13 June 2025
Accepted 14 January 2026
Published 20 February 2026
10.1126/sciadv.adz3026

ScienceAdvances

Structures of the 26*S* proteasome in complex with the Hsp70 co-chaperone Bag1 reveal a mechanism for direct substrate transfer

Moisés Maestro-López, Tat Cheung Cheng, Jimena Muntaner, Margarita Menéndez, Melissa Alonso, Andreas Schweitzer, Masato Ishizaka, Robert J. Tomko, Jr., Jorge Cuéllar, José María Valpuesta, and Eri Sakata

Sci. Adv. **12** (8), eadz3026. DOI: 10.1126/sciadv.adz3026

Science Advances (ISSN 2375-2548) is published by the American Association for the Advancement of Science. 1200 New York Avenue NW, Washington, DC 20005. The title *Science Advances* is a registered trademark of AAAS.